Ain Shams Engineering Journal 17 (2026) 103937

Contents lists available at ScienceDirect

Ain Shams Engineering Journal

journal homepage: www.sciencedirect.com

Full Length Article

Magnetic field effects on the thermo-hydrodynamic behavior of a microscale Tesla valve operating with Fe_3O_4-water ferro-nanofluid

Abderrahim Mokhefi [a], Eugenia Rossi di Schio [b,*], Sarra Youcefi [c], Paolo Valdiserri [b]

[a] Mechanics, Modeling and Experimentation Laboratory L2ME, Faculty of Technology, Bechar University B.P.417, 08000 Bechar, Algeria
[b] Department of Industrial Engineering DIN, Alma Mater Studiorum - University of Bologna, Bologna, Italy
[c] Department of Mechanical Engineering, University of Sciences and Technology of Oran, Oran 31000, Algeria

ARTICLE INFO

Keywords:
microscale Tesla valve
Ferro-nanofluid
Magnetic field
Heat transfer
Flow rectification
Numerical simulation

ABSTRACT

Despite their passive ability to resist reverse flow, Tesla valves can experience altered performance under external influences such as magnetic fields, which can alter or even disrupt the proper functioning of Tesla valves particularly in microscale systems in electronic devices. In this framework, the present study aims to investigate the influence of a horizontal magnetic field on the hydrodynamic and thermal performance of a T45-R microscale Tesla valve integrated into a microsystem. Using computational fluid dynamics (CFD), the effect of the magnetic field, modeled via the Hartmann number (Ha = 0–100), on a laminar (Re = 500) Fe_3O_4-water ferro-nanofluid flow has been analyzed under both forward and reverse flow conditions. The studied flow is governed by the mass, momentum, and energy equations, which has been solved numerically using the finite element method. The results indicate that the magnetic field significantly affects both flow directions, inducing a pressure difference that increases by nearly 150 % for moderate magnetic flux densities (Ha ≈ 25) compared to the non-magnetic case. In forward flow, increased magnetic flux density enhances flow intensity and heat transfer while partially blocking the curved part of the valve, yet it may inadvertently support reverse flow. Diodicity analysis has revealed that valve performance decreases for Hartmann numbers below Ha ≈ 17, independent of nanoparticle concentration, while it improves beyond this threshold. Nevertheless, optimal valve performance is still observed in the absence of a magnetic field.

1. Introduction

In several industrial and microfluidic applications, controlling fluid flow direction without the need for moving parts is a critical challenge [1–3]. Devices such as traditional valves that can efficiently promote forward flow while suppressing reverse flow are essential for improving system reliability, reducing maintenance, and enhancing overall performance. The Tesla valve [4] is a simple yet effective passive flow control element among such devices. Initially invented by *Nikola Tesla* in the early 20th century, the Tesla valve is a fixed-geometry fluidic diode that allows fluid to flow preferentially in one direction without any mechanical components. Its unique design creates asymmetric flow resistance, enabling it to resist backflow while facilitating forward motion, making it particularly attractive in applications ranging from microfluidics and cooling systems to biomedical devices and energy harvesting [5].

Tesla valves have recently attracted growing attention owing to their versatility across a wide range of engineering scales. At the macroscale, they are increasingly integrated into thermal-storage and photovoltaic thermal systems in the energy sector, while in chemical engineering they contribute to enhanced mixing and cavitation-assisted processes [6–8]. Their relevance in thermal management has also grown, driven by optimized geometries that improve heat-sink performance [9]. Extending these advantages to the microscale, Tesla valves are now embedded in electronic cooling devices, lab-on-chip architectures, micropumps, and biomedical microchannels, where reliable passive flow rectification without moving parts is important for stable operation [10].

Due to the complex fluid dynamics within Tesla valves, which create highly complex hydrodynamic architectures, researchers have been motivated to investigate their thermo-hydrodynamic behavior and reliability by modifying valve geometries and studying various influencing factors [11,12]. Indeed, *Purwidyantri and Prabowo* [13] presented a comprehensive review of Tesla valve structures, highlighting their

* Corresponding author.
E-mail addresses: abderrahim.mokhefi@enp-oran.dz (A. Mokhefi), eugenia.rossidischio@unibo.it (E. Rossi di Schio), s_youcefi@yahoo.fr (S. Youcefi), paolo.valdiserri@unibo.it (P. Valdiserri).

https://doi.org/10.1016/j.asej.2025.103937
Received 31 July 2025; Received in revised form 7 December 2025; Accepted 15 December 2025
Available online 30 December 2025

Nomenclature

Symbol

a	Channel section side (m)
B	Magnetic flux density (T)
$\mathbf{B}$	Magnetic field (T)
c	Heat capacity (J kg^{-1} K^{-1})
D	Characteristic diameter (m)
De	Dean number (−)
Di	Diodicity (−)
$\mathbf{f}$	Volume force (N.m^{-3})
F	Dimensionless volume force (−)
g	Gravity (m s^{-2})
Ha	Hartmann number (−)
k	Thermal conductivity (W m^{-1} K^{-1})
L	Channel x-Length (m)
Nu	Nusselt number (−)
p	Pressure (Pa)
P	Dimensionless pressure (−)
Pr	Prandtl number (−)
R	Curved part channel radius (m)
Re	Reynolds number (−)
Ri	Richardson number (−)
S	Surface variable (m^2)
S_0	Channel lateral surface (m^2)
T	Temperature (K)
$\mathbf{u}$	Velocity field (m s^{-1})
$\mathbf{U}$	Dimensionless velocity field (−)
u, v, w	Velocity components (m s^{-1})
U, V, W	Dimensionless velocity (−)
u_0	Inlet velocity (m s^{-1})
x, y, z	Space coordinates (m)
X, Y, Z	Dimensionless space (−)

Greek

α	Thermal diffusivity ($m^2.s^{-1}$)
β	Thermal expansion (K^{-1})
θ	Dimensionless temperature (−)
μ	Viscosity (Pa.s)
ν	Cinematic viscosity (m^2 s^{-1})
ρ	Density (kg m^{-3})
σ	Electrical conductivity (S m^{-1})
φ	Nanoparticles volume fraction

Index

ave	Average
f, p, nf	Fluid, nanoparticles, nanofluid
h, c	Hot, cold
L	Lorentz
r, f	Reverse, forward

renewed relevance in micro- and nanofluidic systems. The work categorizes key designs and discusses their applications as passive components in advanced fluidic technologies.

Truong and Nguyen [14] proposed a comprehensive optimization method for Tesla valves, identifying key geometrical parameters for the first time. Using 2D steady flow simulations, they derived design formulas linked to Reynolds number, enabling systematic valve optimization. *Thompson et al.* [15] evaluated various RANS turbulence models to predict Tesla valve diodicity using 3D CFD simulations for Reynolds numbers up to 2000. Their results show that while the k-ω and SST k-ω models offer good agreement with experiments at moderate Re, the k-ε model significantly underestimates valve performance. *Babaoğlu et al.* [16] optimized multistage Tesla valves by combining simulations with surrogate-based modeling to minimize forward pressure drop and maximize reverse pressure drop. They derived explicit correlations for diodicity as a function of geometric and flow parameters, achieving a maximum diodicity of 1.811 under optimal conditions. *Liu et al.* [17] proposed a symmetric Tesla valve system and investigated its flow and pressure drop characteristics using CFD and dimensional analysis. Their results demonstrate that improved symmetry enhances unidirectional flow behavior. *Zhang et al.* [18] studied the effect of the width-to-narrow ratio on the forward and reverse flow characteristics of a Tesla valve using simulations in the laminar regime, validated by experimental results. They showed that this ratio influences flow distribution and pressure differently depending on the flow direction. *Zeidan et al.* [19] investigated to analyze transient flow and pressure dynamics within Tesla valves, highlighting their role in attenuating pressure surges. The study identifies the formation of pressure pockets as key contributors to non-uniform pressure propagation, offering new insights for valve optimization. Even in aerodynamics, the Tesla valve has demonstrated its presence. Indeed, *Gan et al.* [20] investigated aerodynamic noise reduction in steam-based Tesla valves for nuclear power systems, proposing a progressively expanding structure to mitigate high-temperature, high-pressure effects. CFD analysis revealed that optimized geometric parameters reduce velocity and turbulence while increasing local temperature, significantly suppressing noise generation.

In microscale cooling and heating systems, where fluid flows through complex channels to dissipate heat from sensitive electronics, Tesla valves prevent backflow without mechanical parts [21–26]. Cooling fluids and nanofluids [27], widely employed for their enhanced thermal properties, have also been adopted as working fluids within Tesla valves to improve heat transfer performance and flow control. As the present investigation focuses on nanofluids, so particular attention is given to presenting previous studies in this field. Indeed, nanofluids have proven effective in enhancing heat transfer under ideal operating conditions, motivating studies on their behavior in natural, forced, and mixed convection. CFD analyses [28–30] have employed both 2D and 3D models, while investigations extended to continuous and porous media. In addition to thermal performance, entropy generation has been examined to assess thermodynamic efficiency. These studies underline the versatility and potential of nanofluids for improving heat transfer in diverse engineering applications [31–36].

Despite the growing interest in nanofluids since their inception, research on them within Tesla valves has only recently emerged. Among the earliest studies conducted in this area is that attributed to *Qian et al.* [37]. They numerically studied Al_2O_3-water nanofluid flow through a micro-scale T45-R Tesla valve, analyzing forward and reverse flow behaviors. They found that diodicity is strongly influenced by nanoparticle volume fraction, enhancing flow separation and pressure drop, especially in reverse flow. Using numerical simulations, *Liosis et al.* [38] studied the Tesla valve as a micromixer for mixing Fe3O4 nanoparticles with contaminated water. They found that the Tesla valve geometry can achieve up to 63 % mixing efficiency at a velocity ratio of 20, demonstrating its effectiveness for microfluidic mixing applications. *Soltani et al.* [39] numerically studied multi-stage Tesla valve designs as cooling channels for PEM fuel cells using hybrid nanofluids, showing the reverse valve configuration improved temperature uniformity and increased heat transfer by 15 %. *Shahsavar et al.* [40] numerically investigated the hydrothermal performance and entropy generation of heat sinks with Tesla valve-based helical channels using water-silver nanofluids. Their results show that Tesla valve channels outperform plain helical channels in cooling efficiency and entropy reduction. During this year, work on nanofluids has been carried out by *Ren and Wang* [41]. In their work, they used CFD to analyze the thermal performance of a Tesla valve cold

plate with various nanofluids. They optimized nanofluid parameters, achieving the best heat transfer at 0.13 m/s velocity, 288 K, and 4.38 % volume fraction.

In recent years, magnetohydrodynamics (MHD), which describes the interaction between electrically conductive fluids and external magnetic fields, has garnered significant attention due to its potential in flow control and thermal enhancement [42–48]. This coupling of magnetic forces and fluid dynamics enables researchers to precisely modulate velocity fields and heat transfer characteristics, particularly in microscale systems. The importance of magnetohydrodynamics lies in its ability to induce motion or control the behavior of fluids using magnetic fields [49–51]. Several studies have focused on implementing MHD systems to generate flow or manipulate fluid characteristics in various contexts. For instance, some works have introduced a magnetically actuated pump and micropump to study its influence on microfluidic flows [52,53]. Other investigations have explored the effect of MHD on forced, natural, or mixed convection in confined, porous or continuous media, where buoyancy forces interact with the imposed magnetic field [54–57]. Additionally, MHD has been applied to fluid–structure interaction problems [58–60], marine engineering studies [61], and heat transfer enhancement in micro- and nanoscale systems [62]. More broadly, these studies demonstrate the versatility of MHD in controlling fluid motion, optimizing transport phenomena, and enhancing energy conversion in a wide range of engineering and biomedical applications.

The presence of a Tesla valve in microscale systems, and particularly in electronic devices, raises an important question regarding its operational reliability. Since a Tesla valve passively blocks reverse flow without requiring moving parts, its performance in proximity to sources of magnetic fields may be affected, potentially compromising its ability to prevent backward flow. This concern becomes even more critical when the working fluid is electrically conductive, such as in the case of ferro-nanofluids, where interactions with the magnetic field can modify flow behavior, pressure distribution, and overall diodicity. Therefore, understanding the influence of external magnetic fields on microscale Tesla valves addresses a significant knowledge gap in ensuring their proper functioning in MHD-sensitive environments.

Despite several researchers contributing valuable insights into enhancing the hydrodynamic and thermal performance of Tesla valves, the influence of magnetic field interactions, particularly ferromagnetic nanofluids, remains underexplored. Indeed, although a study on the flow within the Tesla valve using Fe_2O_4 nanoparticles, considered a ferromagnetic fluid, has been conducted by *Liosis et al.* [38], the investigation of the magnetic field effect was not included. This gap is especially critical given that Tesla valves are increasingly integrated into environments exposed to magnetic flux losses, where magnetic field lines can alter flow structure and heat transfer behavior. Such effects may either improve or impair the valve's overall efficiency. In this context, the present work focuses on a numerical investigation of the behavior of a ferromagnetic nanofluid inside a Tesla valve under the influence of a transverse magnetic field. To the best of our knowledge, no prior studies have addressed the combined impact of magnetic fields and ferromagnetic nanofluids in this geometry, highlighting the originality and relevance of our contribution. The present investigation focuses on a specific case involving the application of a magnetic field to the flow of a water-based ferromagnetic nanofluid, in which Fe_3O_4 nanoparticles are suspended. The investigation examines the influence of increasing magnetic flux density and nanoparticle concentration on key behaviors, namely the hydrodynamic and thermal characteristics of both forward and reverse flows within a microscale Tesla valve of type T45-R.Fig. 2.

2. Presentation of the Tesla valve geometry

The valve channel considered in the present study is a microscale Tesla valve of the T45-R type, as previously described by *Truong and Nguyen* [14]. The T45-R Tesla valve consists of three main sections: the inlet, the bifurcation region, and the outlet. Depending on the flow direction, the inlet and outlet sections are interchangeable. The bifurcation zone features a straight and curved (arc-shaped) channel. The flow is considered forward when the fluid enters from the end and is aligned with the straight channel. Conversely, the flow is described as reverse when it enters from the opposite side [14,18,37], see Fig. 2.

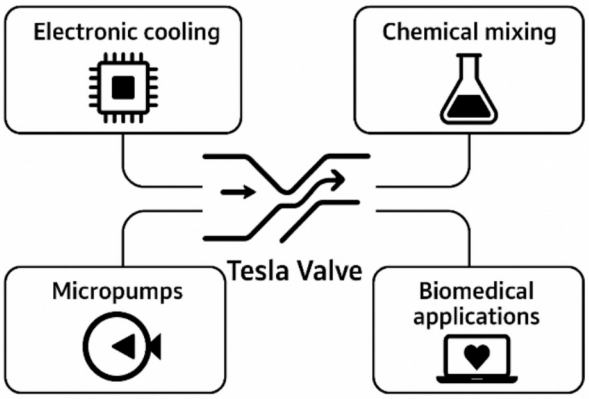

Fig. 1. Overview of Tesla Valve applications across engineering domains.

Fig. 3 shows the horizontal layout of the Tesla valve front section, detailing the geometric dimensions of both the straight and curved channels. It should be noted that the fluid flow cross-section is square-shaped, with side length denoted by *a*.

The various geometrical dimensions illustrated in Fig. 2 are detailed in Table 1. It is noteworthy that *a*, the characteristic length of the Tesla valve, is set to 100 μm, serving as the reference dimension for the entire microchannel structure.

The Tesla valve under investigation is penetrated by a ferromagnetic nanofluid, consisting of a stable suspension of iron oxide nanoparticles (Fe_3O_4) dispersed in pure water. The nanofluid can flow forward and reverse through the valve's asymmetric geometry. A horizontal magnetic field is applied along the X-axis, aligned with the direction of the adjacent straight channel and opposite the curved channel. This magnetic configuration, illustrated in Fig. 4, simulates the influence of magnetic field line losses commonly encountered in electronic environments.

The interaction between the imposed magnetic field and the electrically conductive nanofluid induces a Lorentz force, significantly altering the flow's internal hydrodynamic structure. Moreover, the Tesla

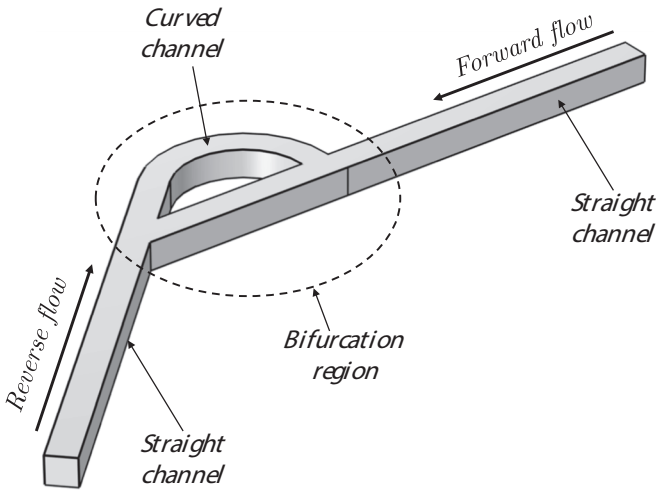

Fig. 2. Presentation of the T45-R Tesla valve geometry.

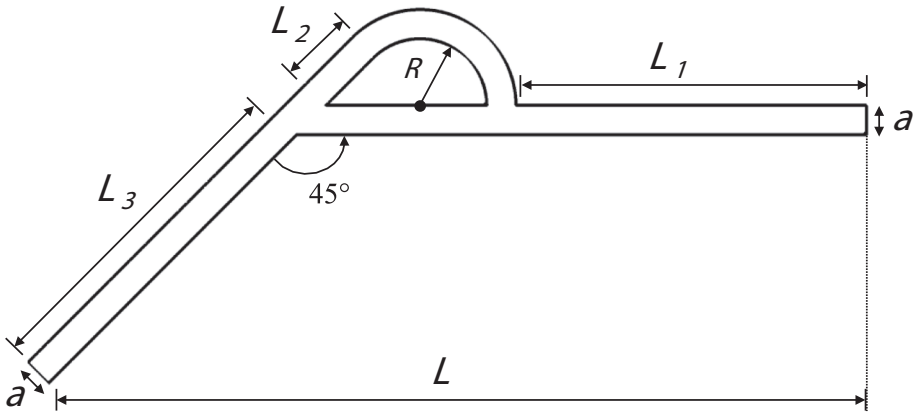

Fig. 3. Presentation of the T45-R Tesla valve geometry.

Table 1
Different geometry dimension ratios of the Tesla valve [18,37].

a [μm]	L_1/a	L_2/a	L_3/a	R/a
100	12	2.35	12	2.28

valve is assumed to operate within a thermally active environment, such as an electronic system, where heat generation causes the valve walls to become thermally energized. Consequently, the nanofluid enters the valve regardless of the flow direction with a lower inlet temperature T_c. It is subject to thermal gradients arising from the hot walls maintained at a temperature T_h. These combined magnetothermal effects result in a complex interplay between heat transfer, magnetic actuation, and directional flow resistance. This makes the system highly relevant for modern thermal management and magneto fluidic applications.

The thermophysical properties of the base fluid (water) and the suspended nanoparticles (Fe_3O_4), including density (ρ), dynamic viscosity (μ) (for water), specific heat capacity (c), thermal conductivity (k), thermal expansion (β) and electrical conductivity (σ), which together define the behavior of the resulting ferromagnetic nanofluid, are summarized in Table 2.

The thermophysical properties of the nanofluid (nf), namely density (ρ_{nf}), viscosity (μ_{nf}), thermal conductivity (k_{nf}), specific heat capacity (c_{nf}), and thermal expansion coefficient (β_{nf}), are calculated based on the nanoparticle volume fraction φ using the thermophysical properties of the base fluid (f) and the nanoparticles (p). To validate the applicability of the adopted correlations, the nanofluid is assumed to behave as a Newtonian and incompressible fluid, maintaining thermal equilibrium with negligible slip velocity between the nanoparticles and the base fluid. Furthermore, the nanoparticles are presumed to be uniformly dispersed within a stable suspension, while interparticle interactions are considered negligible. Based on these assumptions, the classical mixture models used in this study are expressed as follows:

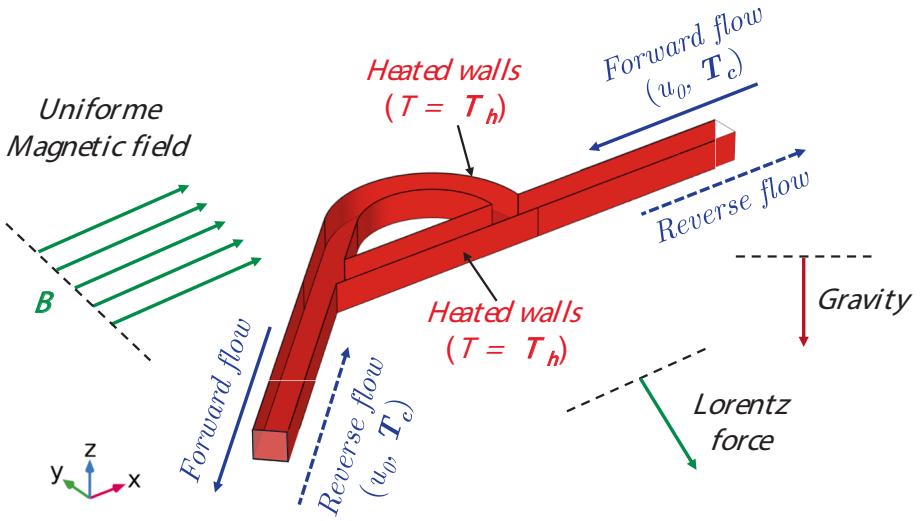

Fig. 4. Schematic of a Tesla Valve under magnetic field and thermal boundary conditions for forward and reverse flows.

Table 2
Thermophysical properties of the nanoparticles and the base fluid [42].

Property	Density [kg/m^3]	Thermal capacity [J/(kg.K)]	Thermal conductivity [W/(m.K)]	Dynamic viscosity [kg/(m.s)]	Thermal expansion [10^{-5}.1/K]	Electrical conductivity [S/m]
Water (f)	1000	4179	0.613	0.001	21.0	0.050
Fe_3O_4 (p)	5200	670.0	06.00	–	1.18	25,000

$$\rho_{\mathrm{nf}} = \varphi\rho_{\mathrm{p}} + (1-\varphi)\rho_{\mathrm{f}} \tag{1}$$

$$\mu_{\mathrm{nf}} = \mu_{\mathrm{f}}(1-\varphi)^{-2.5} \tag{2}$$

$$\frac{k_{\mathrm{nf}}}{k_{\mathrm{f}}} = \frac{k_{\mathrm{p}} + 2k_{\mathrm{f}} - 2\varphi(k_{\mathrm{f}} - k_{\mathrm{p}})}{k_{\mathrm{p}} + 2k_{\mathrm{f}} + \varphi(k_{\mathrm{f}} - k_{\mathrm{p}})} \tag{3}$$

$$(\rho c)_{\mathrm{nf}} = \varphi(\rho c)_{\mathrm{p}} + (1-\varphi)(\rho c)_{\mathrm{f}} \tag{4}$$

$$(\rho\beta)_{\mathrm{nf}} = \varphi(\rho\beta)_{\mathrm{p}} + (1-\varphi)(\rho\beta)_{\mathrm{f}} \tag{5}$$

As for the electrical conductivity of a nanofluid, it is not determined directly through standard correlations. Instead, due to the high electrical conductivity of Fe_3O_4 nanoparticles, the estimation is based on a specific conductivity ratio defined as $\sigma^* = \sigma_f / \sigma_p$. This ratio is then incorporated into the following empirical correlation to estimate the effective electrical conductivity of the nanofluid [42,62].

$$\sigma_{nf} = \sigma_f\left[1 + \frac{3(\sigma^*-1)\varphi}{(\sigma^*+2) - (\sigma^*-1)\varphi}\right] \tag{6}$$

3. Mathematical model

The forward and reverse flow within the Tesla valve can be theoretically described by solving the governing equations of fluid mechanics coupled with heat transfer equations, based on Computational Fluid Dynamics (CFD) principles. Specifically, the flow behavior is governed by the Navier–Stokes equations and the energy equation, which are coupled through the velocity and temperature fields. The influence of the magnetic field is incorporated through the momentum balance by including both the Reynolds and Lorentz forces in the source term of the Navier–Stokes equations. The Lorentz force $\mathbf{f}_L$ acting on the electrically conducting nanofluid is expressed if we consider that u and B are respectively the nanofluid velocity field and magnetic field as:

$$\mathbf{f}_L = \sigma_{nf}(\mathbf{u}\times\mathbf{B})\times\mathbf{B} \tag{7}$$

3.1. Dimensional governing equations

In a Cartesian coordinate system *Oxyz*, as shown in Fig. 3, the flow within the Tesla valve is assumed to satisfy several classical hypotheses. The ferro-nanofluid is modelled as an incompressible and Newtonian effective medium. In addition, the applied magnetic field is considered externally imposed, so that induction effects can be neglected. Furthermore, the flow is assumed to be laminar and steady, while Joule heating is considered negligible. Magnetic effects therefore enter the momentum equation through a magnetic body force for ferrofluids as expressed in **Eq.** (7). The ferro-nanofluid flow is also assumed to be with no chemical reactions, negligible external forces, a dilute nanoparticle concentration, negligible viscous dissipation, negligible radiative heat transfer, and local thermal equilibrium between the nanoparticles and the base fluid. Therefore, given the moderate particle concentration and the negligible slip between nanoparticles and the base fluid, a single-phase approach is sufficient to capture the main hydrodynamic and thermal effects. Consequently, a single-phase model of nanofluid has been considered rather than the two-phase model [63].These assumptions are consistent with standard references in MHD and ferro-nanofluid modelling [42,43]. It should be noted that, all thermophysical properties are considered temperature-independent, except for the density, which is treated as constant throughout the domain except in the buoyancy term of the momentum equation, by the Boussinesq approximation.

Under these assumptions, if $\mathbf{u} = (u, v, w)$, p and T present the velocity field, pressure, and temperature, and the magnetic field of a uniform horizontal flux density B applied according to the x positive direction, the governing equations of the model consist of [63–65].

Mass equation

$$\frac{\partial u}{\partial x} + \frac{\partial v}{\partial y} + \frac{\partial w}{\partial z} = 0 \tag{8}$$

Momentum equations

$$\rho_{nf}\left(u\frac{\partial u}{\partial x} + v\frac{\partial u}{\partial y} + w\frac{\partial u}{\partial z}\right) = -\frac{\partial p}{\partial x} + \mu_{nf}\left(\frac{\partial^2 u}{\partial x^2} + \frac{\partial^2 u}{\partial y^2} + \frac{\partial^2 u}{\partial z^2}\right) \tag{9}$$

$$\rho_{nf}\left(u\frac{\partial v}{\partial x} + v\frac{\partial v}{\partial y} + w\frac{\partial v}{\partial z}\right) = -\frac{\partial p}{\partial y} + \mu_{nf}\left(\frac{\partial^2 v}{\partial x^2} + \frac{\partial^2 v}{\partial y^2} + \frac{\partial^2 v}{\partial z^2}\right) - \sigma_{nf}B^2 v \tag{10}$$

$$\rho_{nf}\left(u\frac{\partial w}{\partial x} + v\frac{\partial w}{\partial y} + w\frac{\partial w}{\partial z}\right) = -\frac{\partial p}{\partial z} + \mu_{nf}\left(\frac{\partial^2 w}{\partial x^2} + \frac{\partial^2 w}{\partial y^2} + \frac{\partial^2 w}{\partial z^2}\right) - \sigma_{nf}B^2 w + \rho_{nf}g\beta_{nf}(T - T_c) \tag{11}$$

Energy equation

$$\rho_{nf}c_{nf}\left(u\frac{\partial T}{\partial x} + v\frac{\partial T}{\partial y} + w\frac{\partial T}{\partial z}\right) = k_{nf}\left(\frac{\partial^2 T}{\partial x^2} + \frac{\partial^2 T}{\partial y^2} + \frac{\partial^2 T}{\partial z^2}\right) \tag{12}$$

It is noted here that, due to the application of the magnetic field in the previously mentioned direction, the Lorentz force **Eq.** (7) introduced in the source term of the momentum equations depends only on the y and z axes, involving only the velocity components v and w, *and* follows:

$$\mathbf{f}_L = \sigma_{nf}(\mathbf{u}\times\mathbf{B})\times\mathbf{B} = -\sigma_{nf}B^2(0, v, w) \tag{13}$$

3.2. Dimensionless governing equations

To conduct a generalized study independent of the system's physical dimensions, it is essential to adopt a non-dimensional strategy. This approach reduces the number of governing parameters and facilitates comparative analysis. To achieve this, the governing equations are dimensionless in a Cartesian coordinate system *OXYZ* using the following non-dimensional (Dimensionless) independent and dependent variables, including position (*X, Y, Z*), velocity $\mathbf{U} = (U, V, W)$, pressure P, and temperature θ expressed as follows [66]:

$$(X, Y, Z) = \frac{(x, y, z)}{D}, (U, V, W) = \frac{(u, v, w)}{u_0}, P = \frac{p}{\rho_{nf}u_0^2} \; and \; \theta = \frac{T - T_c}{T_h - T_c} \tag{14}$$

Here, D represents a characteristic length scale. In our case, the flow cross-section is square, and D is defined as the side length of the square section $D = a$. By substituting these non-dimensional variables **Eq.** (14) into the governing equations **Eqs.** (**8**)-(**12**), the following non-dimensional system is obtained [42,43,62–65]:

Dimensionless mass equation

$$\frac{\partial U}{\partial X} + \frac{\partial V}{\partial Y} + \frac{\partial W}{\partial Z} = 0 \tag{15}$$

Dimensionless momentum equations

$$U\frac{\partial U}{\partial X} + V\frac{\partial U}{\partial Y} + W\frac{\partial U}{\partial Z} = -\frac{\partial P}{\partial X} + \frac{\nu_{nf}}{\nu_f}\frac{1}{\mathrm{Re}}\left(\frac{\partial^2 U}{\partial X^2} + \frac{\partial^2 U}{\partial Y^2} + \frac{\partial^2 U}{\partial Z^2}\right) \tag{16}$$

$$U\frac{\partial V}{\partial X} + V\frac{\partial V}{\partial Y} + W\frac{\partial V}{\partial Z} = -\frac{\partial P}{\partial Y} + \frac{\nu_{nf}}{\nu_f}\frac{1}{\mathrm{Re}}\left(\frac{\partial^2 V}{\partial X^2} + \frac{\partial^2 V}{\partial Y^2} + \frac{\partial^2 V}{\partial Z^2}\right) - \frac{\rho_f}{\rho_{nf}}\frac{\sigma_{nf}}{\sigma_f}\frac{\mathrm{Ha}^2}{\mathrm{Re}}V \tag{17}$$

$$U\frac{\partial W}{\partial X} + V\frac{\partial W}{\partial Y} + W\frac{\partial W}{\partial Z} = -\frac{\partial P}{\partial Z} + \frac{\nu_{nf}}{\nu_f}\frac{1}{\mathrm{Re}}\left(\frac{\partial^2 W}{\partial X^2} + \frac{\partial^2 W}{\partial Y^2} + \frac{\partial^2 W}{\partial Z^2}\right) - \frac{\rho_f}{\rho_{nf}}\frac{\sigma_{nf}}{\sigma_f}\frac{\mathrm{Ha}^2}{\mathrm{Re}}W + \frac{(\rho\beta)_{nf}}{\rho_{nf}\beta_f}\mathrm{Ri}\theta \tag{18}$$

Dimensionless energy equation

$$U\frac{\partial\theta}{\partial X}+V\frac{\partial\theta}{\partial Y}+W\frac{\partial\theta}{\partial Z}=\frac{\alpha_{nf}}{\alpha_f}\frac{1}{\mathrm{Re}Pr}\left(\frac{\partial^2\theta}{\partial X^2}+\frac{\partial^2\theta}{\partial Y^2}+\frac{\partial^2\theta}{\partial Z^2}\right) \tag{19}$$

The dimensionless numbers appearing in the governing Navier-Stokes and energy equations, **Eqs. (15)-(19)** include the Reynolds number (Re), the Richardson number (Ri), the Hartmann number (Ha), and the Prandtl number (Pr). These are respectively defined as follows:

$$\mathrm{Re}=\frac{\rho_f u_0 D}{\mu_f},\mathrm{Ri}=\frac{g\beta_f(T_h-T_c)}{u_0^2},\mathrm{Ha}=BD\sqrt{\frac{\sigma_f}{\mu_f}}\ and\ \mathrm{Pr}=\frac{\nu_f}{\alpha_f} \tag{20}$$

On the other hand, α and ν for both base fluid (f) and nanofluid (nf) represent the thermal diffusivity and the kinematic viscosity, respectively, defined as follows:

$$\alpha=\frac{k}{\rho c}\ and\ \nu=\frac{\mu}{\rho} \tag{21}$$

In certain studies, involving curved channels, the introduction of Dean numbers is necessary to characterize the formation of transverse vortices, commonly referred to as Dean vortices. This dimensionless number is defined as follows:

$$De=\mathrm{Re}\sqrt{\frac{2a}{R}} \tag{22}$$

It should be noted here that, according to the dimensionless model provided, the dimensionless Lorentz force $\mathbf{F}_L$ is expressed as follows:

$$\mathbf{F}_L=-\frac{\rho_f}{\rho_{nf}}\frac{\sigma_{nf}}{\sigma_f}\frac{\mathrm{Ha}^2}{\mathrm{Re}}(0,V,W)\Rightarrow\|\mathbf{F}_L\|=\frac{\rho_f}{\rho_{nf}}\frac{\sigma_{nf}}{\sigma_f}\frac{\mathrm{Ha}^2}{\mathrm{Re}}\sqrt{V^2+W^2} \tag{23}$$

3.3. Boundary conditions

The governing equations describing the steady-state flow of the ferromagnetic nanofluid within the Tesla valve are supplemented by appropriate boundary conditions to enable numerical resolution. According to the boundary configuration illustrated in Fig. 4, a uniform inlet velocity u_0 and a cold temperature T_c are imposed at the entrance, regardless of whether the flow is in the forward or reverse direction. No-slip boundary conditions are applied along the channel walls, which are maintained at higher temperatures, T_h. At the outlet, symmetry boundary conditions are assumed. These boundary conditions in the dimensionless form, based on the dimensionless variables, can be expressed as follows [37]:

- At the channel forward flow inlet ($X=L$):

$$U=-1,\ V=0,\ W=0\ and\ \theta=0 \tag{24}$$

- At the channel reverse flow inlet ($X+Y=0$):

$$U=V=\frac{\sqrt{2}}{2},\ W=0\ and\ \theta=0 \tag{25}$$

- At the channel walls:

$$U=V=W=0\ and\ \theta=1 \tag{26}$$

- At the channel forward flow outlet ($X+Y=0$):

$$\frac{\sqrt{2}}{2}\left(\frac{\partial}{\partial X}+\frac{\partial}{\partial Y}\right)(U,V,W)=0\ and\ \frac{\sqrt{2}}{2}\left(\frac{\partial\theta}{\partial X}+\frac{\partial\theta}{\partial Y}\right)=0 \tag{27}$$

- At the channel reverse flow outlet ($X=L$):

$$\frac{\partial U}{\partial X}=\frac{\partial V}{\partial X}=\frac{\partial W}{\partial X}=0\ and\ \frac{\partial\theta}{\partial X}=0 \tag{28}$$

3.4. Tesla valve flow efficiency

In Tesla valve efficiency, key performance indicators are employed to highlight the valve's overall hydraulic behavior and effectiveness. One of the most significant parameters is the pressure drop between the inlet and outlet of the channel. This quantity is obtained from the pressure distribution along the main flow path and is calculated for both the forward and reverse flow scenarios. The dimensionless pressure drops for both forward (ΔP_f) and reverse (ΔP_r) flows are given by [37]:

$$\Delta P_f=P_{Inlet,f}-P_{Outlet,f}and\ \Delta P_r=P_{Inlet,r}-P_{Outlet,r} \tag{29}$$

Our study's analysis has been based on relative dimensionless pressure, where the outlet dimensionless pressure has been set to zero (non-dimensional as 0 Pa). Consequently, the dimensionless pressure drop effectively corresponds to the dimensionless pressure at the inlet.

$$\Delta P_f=P_{Inlet,f}\ and\ \Delta P_r=P_{Inlet,r} \tag{30}$$

Another key characteristic in the study of Tesla valves is diodicity (Di), which quantifies the rectification performance of the valve by comparing its resistance to forward and reverse flows. It is defined as the ratio of the dimensionless pressure drop in the reverse direction to that in the forward direction under the same inlet conditions, given by [37]:

$$\mathrm{Di}=\frac{\Delta P_r}{\Delta P_f}=\frac{P_{Inlet,r}}{P_{Inlet,f}} \tag{31}$$

A diodicity Di greater than 1 indicates the valve's ability to impede reverse flow more effectively than forward flow, thus mimicking the function of a fluidic diode. This dimensionless parameter is essential for evaluating the asymmetric flow behavior that underpins the passive control mechanism of Tesla valves.

3.5. Tesla valve thermal efficiency

The heat transfer efficiency in the Tesla valve is generally assessed by the convective heat transfer rate, which is expressed in dimensionless form through the variation of the local Nusselt number along the heated walls of the Tesla valve. In the present case, these walls refer to the internal surfaces of the valve excluding the inlet and outlet sections. The local Nusselt number provides insight into the dominance of convection over thermal conduction within the nanofluid and is defined by the following expression:

$$\mathrm{Nu}=-\frac{k_{nf}}{k_f}\frac{\partial\theta}{\partial N} \tag{32}$$

In this expression, N denotes the dimensionless normal vector. To assess the overall heat transfer rate more generally, an averaging operation of the local Nusselt number over the heated wall can provide valuable insight into the global thermal efficiency. It is given by:

$$\mathrm{Nu}_{ave}=\frac{1}{S_0}\int_{\text{hot walls}}Nu\ \mathrm{d}S \tag{33}$$

With S_0 representing the surface of the hot walls, the Tesla valve, and S denotes the variable of surface.

4. Numerical resolution steps

4.1. Resolution step

The nondimensional governing equations **Eqs. (15)-(19)**, coupled with the appropriate boundary conditions, **Eqs. (24)-(28)** to capture both forward and reverse flow regimes within the Tesla valve have been solved numerically using the Galerkin finite element method (FEM). The resolution process begins with transforming the strong form of the partial differential equations into their corresponding weak formulation by multiplying each governing equation by suitable test functions and

integrating over the computational domain. This step allows the accommodation of boundary conditions in a natural manner and reduces the differentiability requirements on the solution.

Following the variational formulation, the domain has been discretized into a finite number of subdomains (elements), over which polynomial basis functions have approximated the solution variables. The discretization procedure leads to assembling a global system of algebraic equations, where local element matrices and vectors are systematically combined according to the mesh connectivity to form a sparse linear system.

For the temperature field, this resulting linear system has been solved using a direct solver of the Paradiso type, ensuring robustness and accuracy in obtaining the thermal distribution. Conversely, the coupled hydrodynamic variables, including velocity and pressure, have been computed via an iterative approach based on the Successive Over-Relaxation (SOR) method. This iterative scheme is well-suited for solving the large sparse linear systems arising from discretizing the incompressible Navier-Stokes equations, offering improved convergence efficiency by optimally tuning the relaxation parameter.

For the first iteration of our numerical scheme, the initial conditions have been chosen based on the three independent variables of the problem: velocity, pressure, and temperature. The velocity and pressure fields were initialized to zero throughout the domain. The temperature field, however, has been initialized using a mean value between the hot and cold temperatures, i.e., $(T_h + T_c)/2$ in the dimensional case. In the dimensionless formulation, this value has been set to 0.5 to accelerate convergence toward the steady-state solution. The relative error has been initially set to a relatively large value to allow the iterative process to converge. Convergence has been achieved when the relative error in all variables dropped below $\varepsilon = 10^{-5}$, ensuring a sufficiently accurate solution. If ψ represents a dependent variable (Velocity, pressure or temperature) and n the iteration order, the relative error is given by:

$$\frac{|\psi^{n+1} - \psi^{n}|}{|\psi^{n+1}|} \prec \varepsilon \tag{34}$$

4.2. Mesh description and check

The mesh employed in this study is predominantly tetrahedral through the entire computational domain, except near the no-slip walls, where a boundary layer mesh comprising three layers of prismatic elements has been implemented. This prism-layer refinement strategy has been specifically designed to accurately resolve the hydrodynamic and thermal boundary layers, enhancing the precision of computed normal gradients of key quantities such as the Nusselt number. The structured prismatic layers ensure better mesh quality and numerical stability in regions with steep gradients adjacent to solid boundaries, see Fig. 5.

The direct use of mesh in such a study presents a critical step that requires a thorough mesh independence test to ensure that a further increase in the number of elements does not significantly affect the numerical results. Thus, a mesh sensitivity analysis was conducted employing three meshes (Mesh 1, 2 and 3) with progressively increasing element numbers while maintaining the same mesh structure described previously. This analysis focused on monitoring the evolution of key output parameters, specifically the diodicity and the average Nusselt number, under both forward and reverse flow conditions.

The details of the mesh test are summarized in Table 3. The data shows that the Mesh 2 consisting of approximately 3,774,055 elements provides sufficient resolution for reliable simulation results. It should be noted that the mesh independence test has been performed for the most demanding case scenario, characterized by highly disturbed flow conditions approaching turbulence, with the Reynolds number fixed at Re = 500, Hartmann number at Ha = 0, and nanoparticle volume fraction set to $\varphi = 0.04$. We further verified that the mesh test results remain robust and valid under these stringent conditions across the entire parameter space investigated, including variations in Hartmann number and nanoparticle concentration.

The absolute error tolerance between successive iterations of the computed variables has been set to 10^{-5}. Regarding the mesh sensitivity test, the results have been considered stable when the absolute error between two successive meshes did not exceed 10^{-3}.

4.3. Comparison with other studies in the literature

Following a mesh independence test, the comparison step remains essential to ensure that the obtained numerical results are reliable and consistent with published data. To reinforce the credibility of the present approach, we validated the present model against the reference study of *Qian et al.* [37], which examined nanofluid flow under comparable conditions using an alumina-water nanofluid. Several hydrodynamic fields and pressure distributions were compared, as illustrated in Figs. 6 and 7.

According to Fig. 6, the velocity profiles and streamline patterns obtained using our simulation with the optimal mesh (Mesh 2), defined in the previous subsection, match almost perfectly those reported in the reference study, regardless of the flow direction (forward or reverse). This demonstrates that the selected mesh not only ensures numerical stability but also accurately captures the essential flow features.

Furthermore, to provide a more rigorous validation, the pressure distribution (see Fig. 7) along the straight channels in both flow directions has been compared not only with the reference data [37] but also across all meshes used in the sensitivity analysis (Mesh 1, 2, and 3). This additional comparison strengthens the evaluation process by

Table 3
Mesh test in the case of Re = 100, Pr = 6.8, Ha = 0, and $\varphi = 0.04$.

Mesh	Mesh 1	Mesh 2	Mesh 3
Elements	776,676	3,774,055	4,201,109
Diodicity (Di)	1.0838	1.0841	1.0841
Average Nusselt number (f)	8.5403	9.8549	9.8550
Average Nusselt number (r)	10.631	10.631	10.631

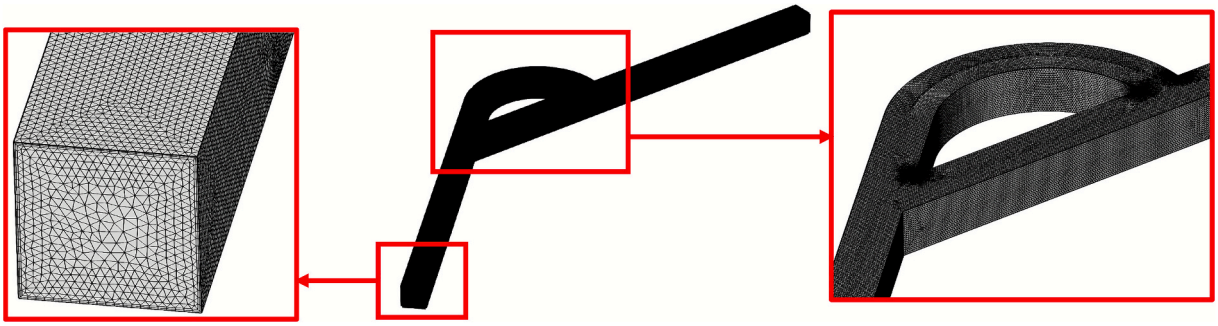

Fig. 5. Mesh of Tesla Valve computational domain.

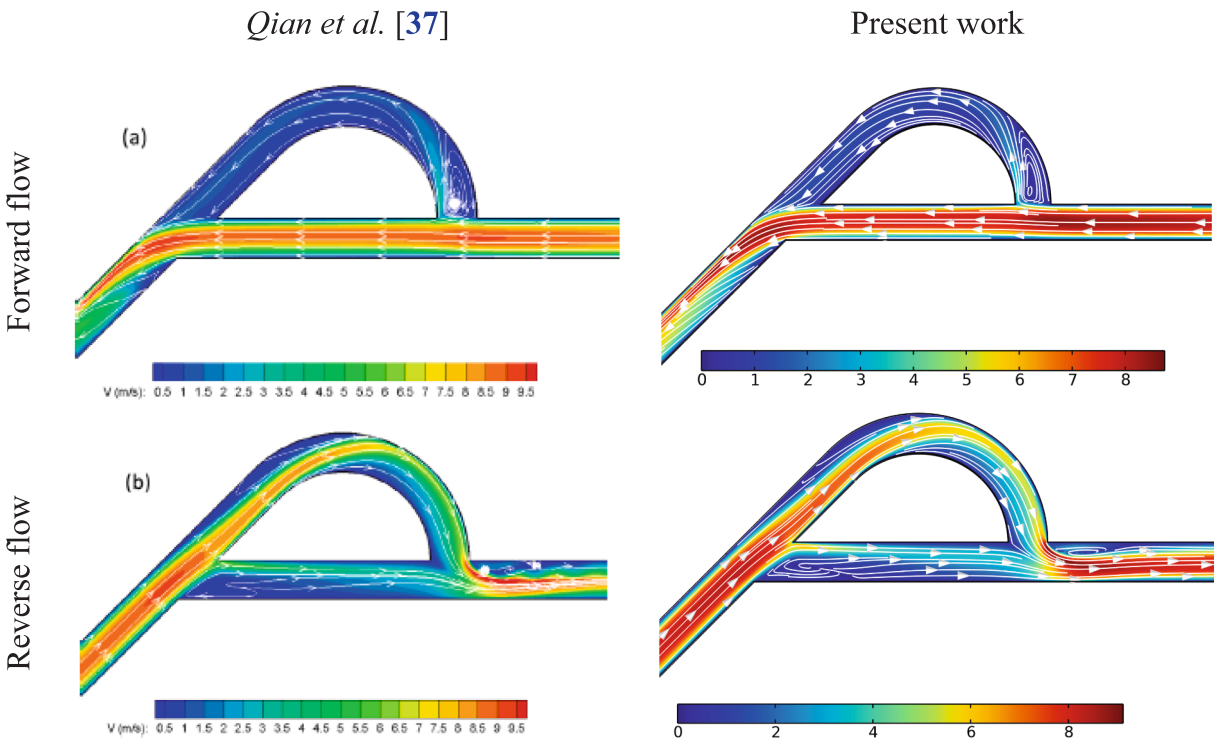

Fig. 6. Comparison of the velocity and streamlines of the present numerical code with those of Qian et al. [37].

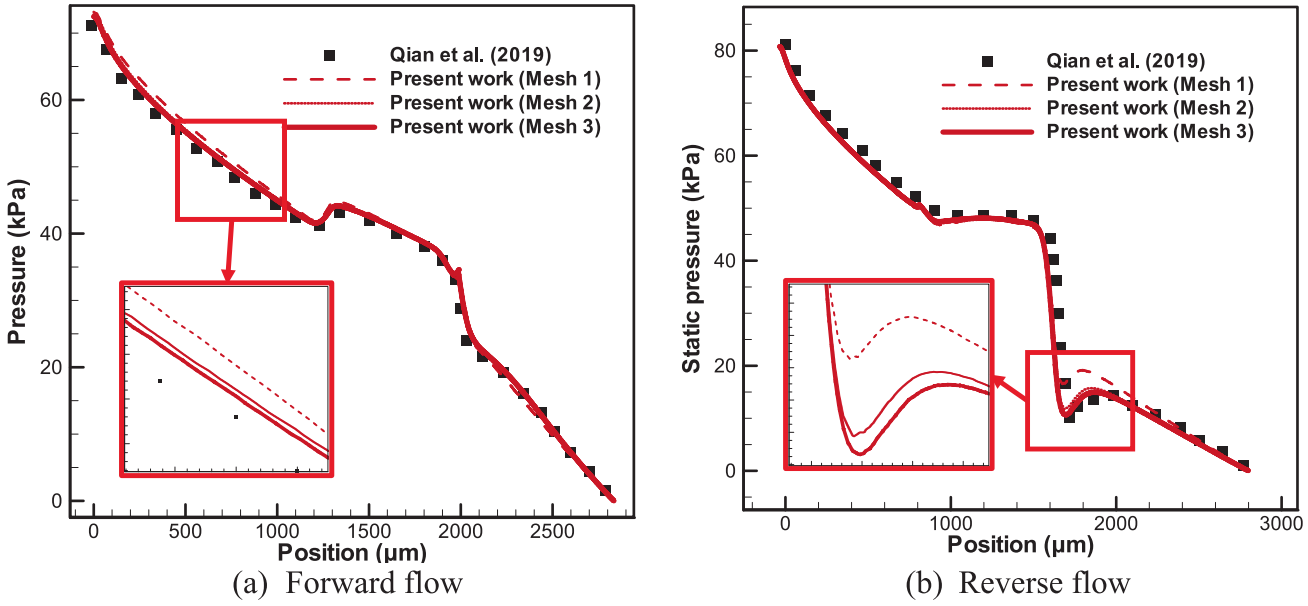

Fig. 7. Comparison of the static pressure of the present numerical code with that of Qian et al. [37].

showing the impact of mesh refinement on the resulting pressure fields. As observed, the optimal mesh (Mesh 2) (which already proved its efficiency in the mesh independence test) also exhibits the highest level of agreement with the reference results. For this mesh, the predicted pressure distribution is nearly identical to that of the reference, with deviations remaining below 1 %.

5. Results and discussion

This section presents and discusses numerical results obtained from the simulation of laminar flow through the micro-scale T45 Tesla valve. Both flow directions, forward and reverse, have been considered to investigate the hydrodynamic and thermal behavior under varying conditions. The analysis has been carried out by examining the velocity, temperature fields, and pressure losses along the main channel in both configurations. The Reynolds number has been kept constant at Re = 500 for all simulations. In contrast, the Hartmann number has been treated as the key variable, being varied from Ha = 0, corresponding to the absence of a magnetic field, up to Ha = 100, to assess the influence of a horizontal magnetic flux density on flow behavior. Furthermore, the effect of the nanoparticle volume fraction has been evaluated, with particular emphasis on its role in modifying the diodicity of the valve

and enhancing the global heat transfer, as quantified by the average Nusselt number. It should be noted, that in this study, only the effect of the forced convection has been considered, thus the Richardson number has been set to be Ri = 0.

Fig. 8 illustrates the reference planes adopted to present the Tesla valve cavity's flow and thermal field distributions. A horizontal mid-plane $Z = 0.5$, corresponding to the longitudinal symmetry axis of the main channel, has been selected to analyze the core flow structure. In addition, vertical planes intersecting the curved and the right sections of the valve, $X = 12.6$ and $Y + X = 12$, have been considered to capture the formation of Dean vortices resulting from the curvature-induced secondary flows and complex magnetohydrodynamic flow.

5.1. 3D stream analysis

Based on the simulations, the ferromagnetic nanofluid flow streamlines within the Tesla microvalve channel have been plotted for various magnetic field intensities. Fig. 9 presents the streamline patterns, colored by the dimensionless velocity magnitude $||\mathbf{U}|| = (U^2 + V^2 + W^2)^{1/2}$, for both forward and reverse flow configurations. In this case, the Reynolds number has been fixed at Re = 500, while a moderate magnetic flux density corresponding to a Hartmann number of Ha = 25 has been imposed.

In both flow directions, the presence of the magnetic field has led to a complex hydrodynamic structure within the channel, particularly in the curved section of the Tesla valve, where the flow becomes three-dimensionally vortical. In the case of reverse flow, a pseudo-stagnation has been observed in the curved region, where the magnetic field appears to inhibit the flow. The dimensionless velocity magnitude in this zone is low, indicating strong suppression of motion.

These observations are in direct correlation with the action of the Lorentz force $\mathbf{F}_L$ which acts normal to the flow field, generated by applying a uniform horizontal magnetic field, see Fig. 10. Its influence is particularly evident in the region where the main channel transitions into the curved segment, where the magnetic flux density exhibits significant spatial variation, leading to increased resistance to fluid motion and altered streamline behavior. It is also noted that the direction of the dimensionless Lorentz force is reversed between the forward and reverse flow cases.

5.2. Forward flow analysis

The forward flow represents the direction in which the Tesla valve is intended to facilitate fluid motion with minimal resistance. In the present configuration, analyzing the hydrodynamic and thermal behavior of a ferromagnetic nanofluid under an applied magnetic field provides a reference baseline for comparison with the reverse flow regime. This investigation is particularly relevant for electronic cooling applications, where Tesla valves help enhance heat dissipation in terms of suppressing undesired back-flow in microscale channels. In this context, the forward-flow analysis reveals how the magnetic field reorganizes streamlines, modifies the pressure distribution, and affects convective heat transfer.

Fig. 11 illustrates the pattern of streamlines for various magnetic flux densities, corresponding to Hartmann numbers of 0, 25, and 100. It is first observed that the highest dimensionless velocity occurs when the Hartmann number is Ha = 100, particularly at the junction between the two straight channels of the Tesla valve. In addition, more flow stagnation (velocity reduction) is observed in the case of the highest Hartmann number (Ha = 100). In the latter case, a significant vortical flow is observed in the second straight channel compared to the standard case (Ha = 0). However, to gain more comprehensive insights into the flow behavior, it becomes essential to examine further the structure of the streamlines, velocity, and temperature profiles across multiple planes as presented in Fig. 8.

Fig. 12 presents the distribution of dimensionless velocity magnitude accompanied by streamlines and the dimensionless temperature field plotted over the horizontal mid-plane of the device (see Fig. 8. **(a)**) for various Hartmann numbers under forward flow conditions.

In the case of the absence of the magnetic field (Ha = 0), the flow is primarily directed through the straight channel, while it is almost entirely blocked in the curved part of the channel. A significant vortex structure has been observed at the bifurcation leading into the curved duct, indicating a considerable pressure loss that restricts fluid motion through the curved path. As a result, a high flow rate is directed along the main straight channel. This flow behavior is also reflected in the thermal field, which appears to be strongly influenced by the flow distribution. Indeed, the incoming cold fluid is primarily guided through the straight section, whereas the relatively hotter region is concentrated within the curved channel, where flow stagnation occurs.

Upon the application of a magnetic field, significant changes in the flow structure have been observed. First, the stagnation of fluid in the curved part of the valve has become more pronounced due to a notable reduction in dimensionless velocity within that region. Although the intensity of the vortex initially formed at the entrance of the curved branch has decreased, the dimensionless velocity has been almost entirely decreased (even canceled), giving rise to a large, stagnant vortex. This vortex forms a dead zone, localized in the middle of the curvature. On the other hand, a strong disturbance in the streamlines has also been observed in the curved section near the outlet bifurcation, indicating flow separation and reorganization. In addition, a high-inertia zone has formed at the corner between the two straight channels, near the outlet bifurcation. This region exhibits the highest local dimensionless velocity among all examined cases, even exceeding that of the magnetic field absence.

However, when comparing the overall flow behavior at this plane, it has been found that the global dimensionless velocity level is lower in the presence of a magnetic field than in its absence. These alterations in the flow field are directly attributed to the action of the Lorentz force, which (depending on its local direction) disrupts the flow distribution and enhances fluid stagnation within the curved segment, as previously illustrated in Fig. 10.

Regarding the dimensionless temperature distribution, the imposition of a magnetic field has been found to alter the thermal field in a manner consistent with the modified dimensionless velocity profile. In particular, for higher magnetic flux densities such as in the case of Ha = 100 an accumulation of hot fluid is clearly observed within the curved

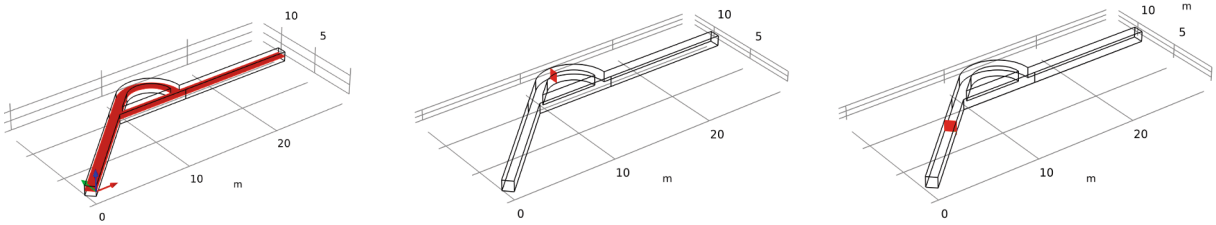

Fig. 8. Principal measurement planes.

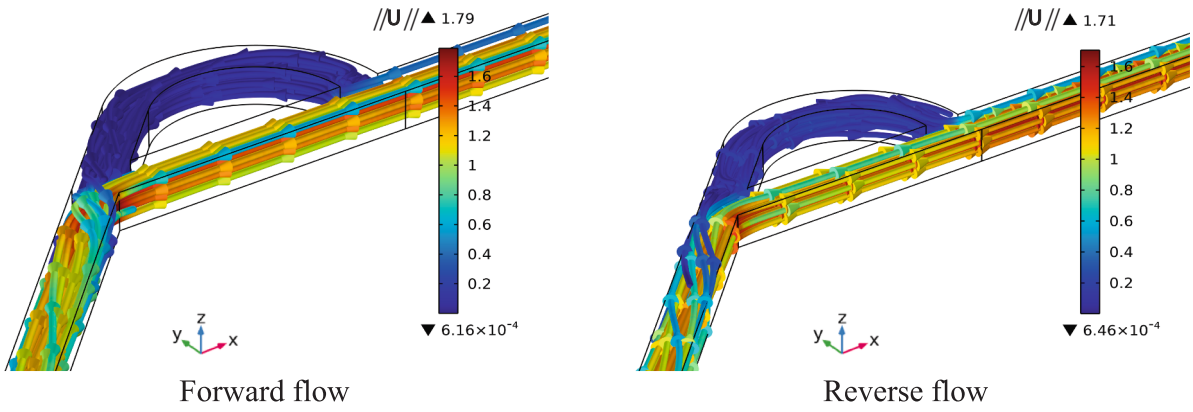

Fig. 9. Flow streamlines colored with the dimensionless velocity magnitude in the case of forward and reverse flow for Ha = 25, Re = 500, Ri = 0, and φ = 0.04.

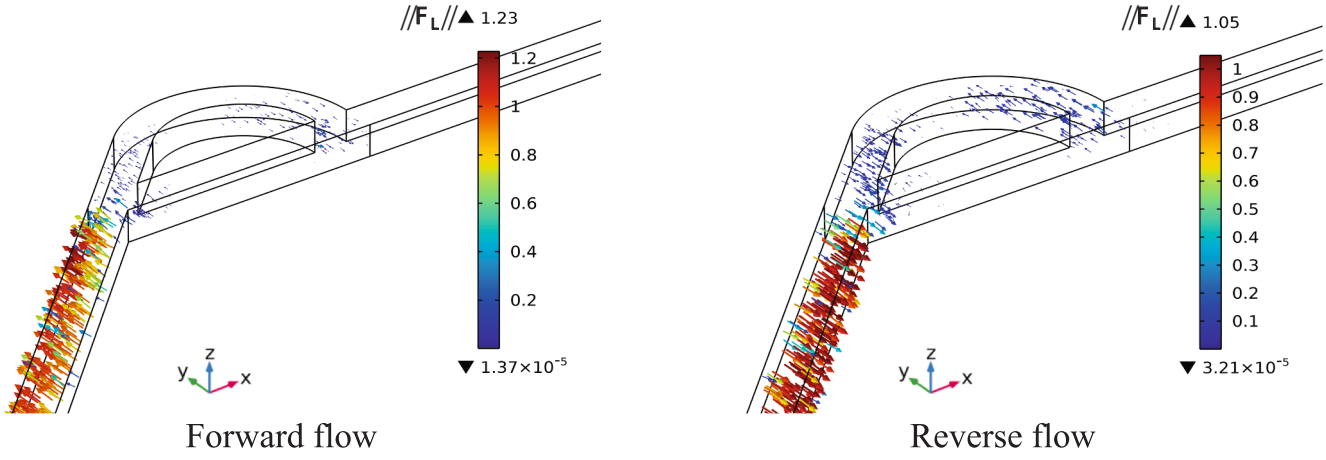

Fig. 10. Dimensionless Lorentz force field for forward and reverse flow for Ha = 25, Re = 500, Ri = 0, and φ = 0.04.

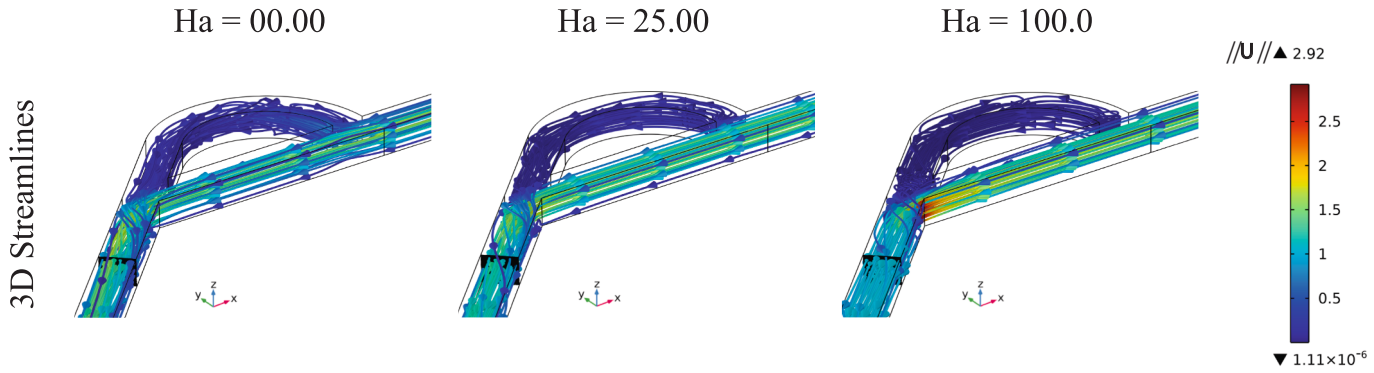

Fig. 11. Flow streamlines colored with the dimensionless velocity magnitude in the case of forward flow for different Hartmann numbers at Re = 500, Ri = 0, and φ = 0.04.

branch of the valve, indicating reduced convective transport in that region. In this situation, the accumulation of hot fluid within the curved section of the channel can significantly reduce the cooling efficiency, particularly in electronic thermal management systems. This localized overheating limits heat dissipation near the region adjacent to the valve curvature. Therefore, for such applications, an additional protection against magnetic-field leakage is recommended to ensure that the Tesla valve maintains its intended role of suppressing reverse flow. This also helps prevent any undesired magnetic interaction with the working ferrofluid, thereby preserving both flow stability and thermal performance.

The flow within the Tesla valve also requires investigation through transverse cross-sections. Therefore, we have selected two planes that have been previously defined (see Fig. 8). The first transverse plane intersects the midpoint of the curved section of the valve. At the same time, the second is located along the straight channel directly connected to the curvature, representing the outlet region of the device.

Fig. 13 illustrates the fluid dimensionless velocity, streamlines, and thermal distribution across the plane (2), see Fig. 8**. (b)**. In the absence of a magnetic field, high dimensionless velocities have been observed within the curved part of the duct, accompanied by the formation of Dean vortices (De = 468.29), indicating a flow with significant inertial

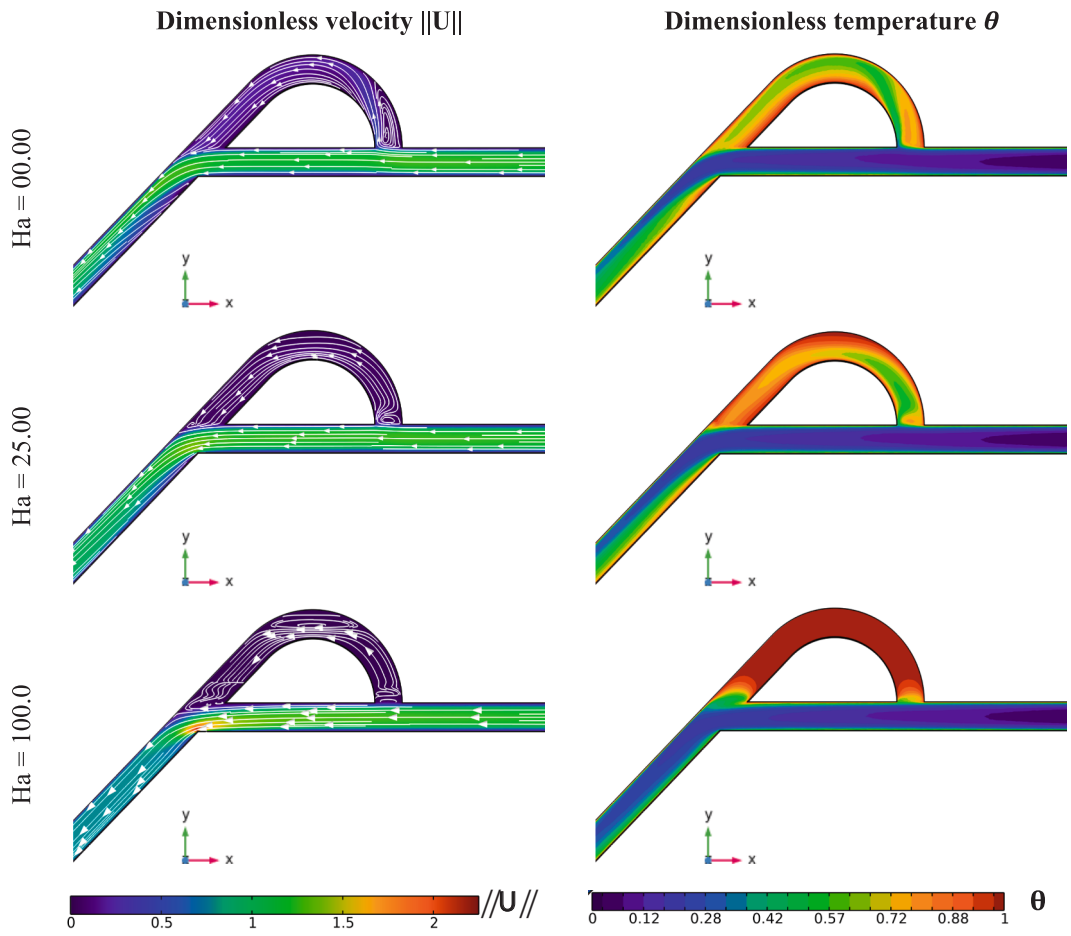

Fig. 12. Dimensionless velocity and temperature profiles in the measurement plane (1) in the case of forward flow for different Hartmann numbers at Re = 500, Ri = 0 and φ = 0.04.

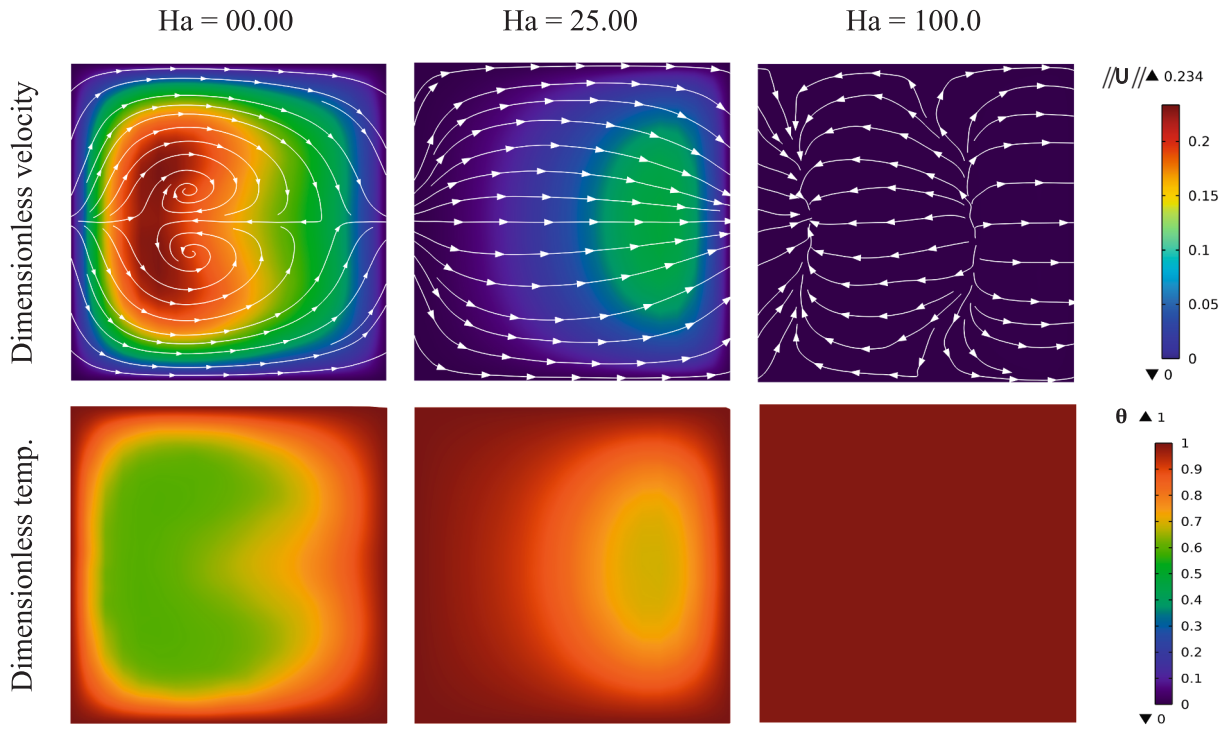

Fig. 13. Dimensionless temperature distribution in the measurement plane (2) in the case of forward flow for different Hartmann numbers at Re = 500, Ri = 0, and φ = 0.04.

effects. When a magnetic field has been applied, a notable dimensionless velocity reduction occurred in this region, consistent with the observations previously made in the horizontal plane (Fig. 12). As a result, Dean vortices have been suppressed, and the flow became dominated by magnetically induced vortices, following the orientation of the Lorentz force. This highlights that the Dean number, which governs the formation of Dean vortices, satisfies the condition for their development in the non-magnetic case but decreases significantly with increasing magnetic flux density. Regarding the dimensionless temperature distribution at this plane, it has been observed that the thermal and hydrodynamic behaviors exhibit similar patterns. Moreover, introducing a magnetic field leads to a more homogeneous hot fluid distribution, thereby promoting hot fluid accumulation and activating thermal conduction within the curved region.

Fig. 14 illustrates the hydrodynamic and thermal profiles for different Hartmann numbers at the plane (3), see Fig. 8**. (c).** It has been observed that Dean vortices develop in this straight section, regardless of the Hartmann number. Although the channel is not curved at this location, the effect of the upstream bend, combined with interference from the flow emerging from the curved section, induces spiral vortex structures, as previously identified in Fig. 9. These structures are typical of Dean-type vortices, manifested as two co-rotating vortex pairs. With increasing Hartmann number, the intensity of these vortices gradually weakens but does not vanish completely. This persistence is attributed to the residual inertial effects and the geometric memory of the flow, where the upstream curvature still imparts a rotational tendency, and the Lorentz force, while damping the motion, is insufficient to entirely suppress secondary flow structures in regions of strong momentum transfer.

Regarding the dimensionless temperature field, it is observed that the increase in the Hartmann number enhances the transport of cold fluid within this region. Indeed, the blue area, indicating lower dimensionless temperatures, expands significantly across the section as the magnetic field intensifies. Simultaneously, the thermal boundary layer becomes thinner, which implies an increase in heat transfer effects and a more uniform dimensionless temperature distribution driven by the flow restructuring under the influence of the Lorentz force, see also Fig. 12.

To better assess the global impact of the Hartmann number on the flow behavior in the forward direction through the Tesla valve, it is essential to analyze the dimensionless pressure distribution along the centerline connecting the two straight ducts, deliberately excluding the curved section. This analysis is important in understanding the magnetic field's influence on hydrodynamic resistance.

Fig. 15 illustrates the dimensionless pressure distribution along this reference line for various Hartmann numbers. It is observed that, regardless of the Hartmann number, the most significant dimensionless pressure drops occurs near the outlet straight channel part (zone 1), where the decrease is notably sharper than in the inlet region (zone 2 and 3). Furthermore, increasing the Hartmann number from 0 to 100 leads to a remarkable rise in overall maximal dimensionless pressure levels. Specifically, dimensionless pressure values at the inlet increase from around 4 (Ha = 0) to approximately 120 (Ha = 100). In fact, this important rise in dimensionless pressure difference (ΔP) is fully consistent with the strong intensification of the magnetic field, which in this study reaches a relatively high Hartmann number of Ha = 100. For more moderate magnetic-field strengths, however, the dimensionless pressure increase remains less pronounced. For instance, at Ha = 25, the inlet dimensionless pressure rises from a value close to 4 (Ha = 0) to approximately 10, meaning that the dimensionless pressure level is improved of about 150 %, which confirms that even moderate magnetic flux densities substantially reinforce the magnetic braking effect and consequently elevate the required dimensionless pressure to drive the ferrofluid through the valve. This substantial change highlights that the Lorentz force significantly resists the forward flow, dramatically enhancing the pressure difference across the Tesla valve.

This increase in inlet static dimensionless pressure, induced by the rising Hartmann number, is not considered detrimental in the present configuration. In contrast, it highlights the effective influence of the Lorentz force on the flow field, acting as a resistive mechanism that stabilizes and redirects the fluid motion. The resulting pressure rise compensates for the magnetic braking, ensuring the flow continues despite increased opposition. Therefore, this behavior confirms the magnetic field's role in enhancing flow control within the Tesla valve, particularly in promoting directional selectivity and reducing undesired recirculation loops.

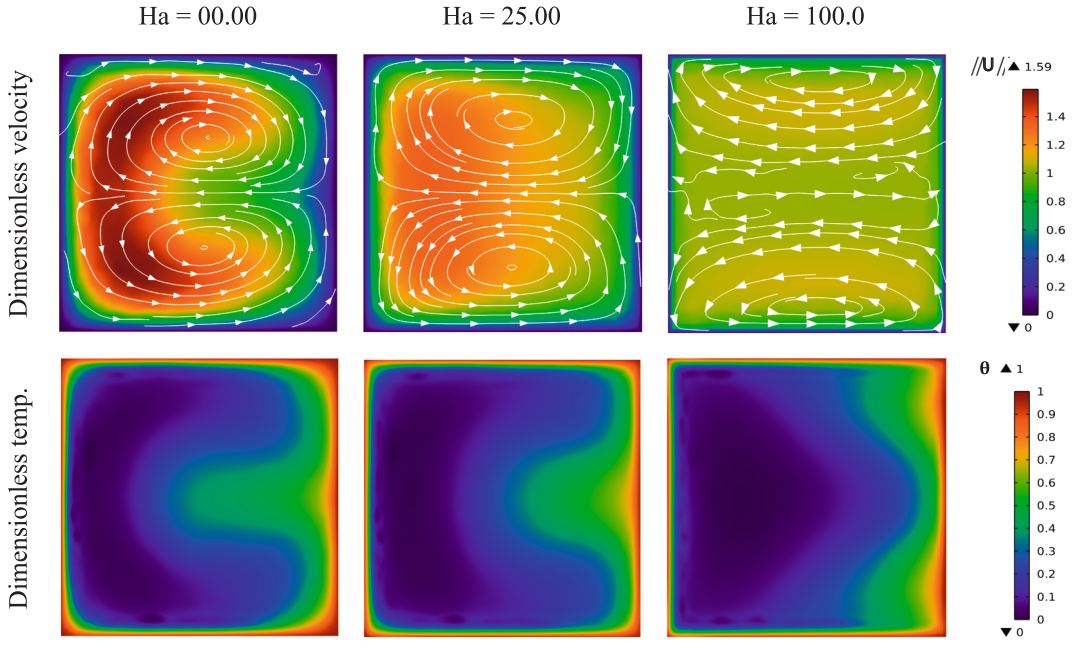

Fig. 14. Dimensionless temperature distribution in the measurement plane (3) in the case of forward flow for different Hartmann numbers at Re = 500, Ri = 0, and φ = 0.04.

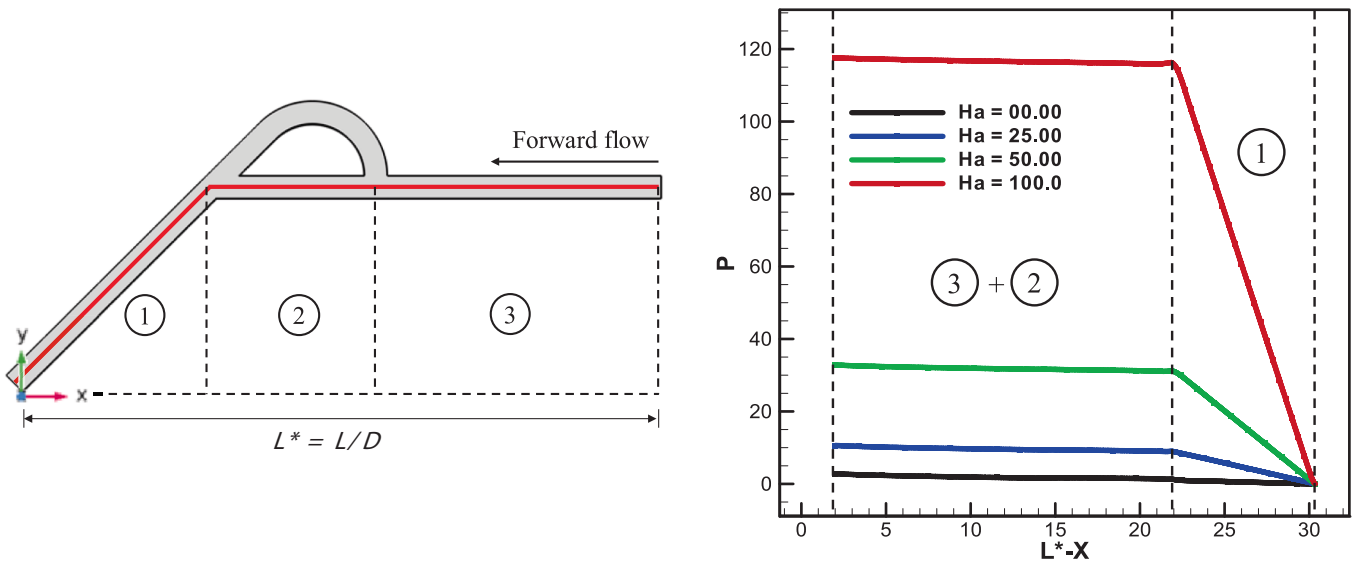

Fig. 15. Dimensionless pressure distribution along the measurement line in the case of forward flow for different Hartmann numbers at Re = 500, Ri = 0, and φ = 0.04.

5.3. *Reverse flow analysis*

To understand the flow behavior inside the Tesla valve under magnetic influence, it is essential to investigate not only the forward flow configuration but also the reverse flow condition. The asymmetric geometry of the Tesla valve inherently causes distinct flow features depending on the direction of the fluid. Therefore, analyzing the magnetic field's effect in the reverse flow case is important, as it may lead to different hydrodynamic responses, vortex formations, and thermal transport mechanisms compared to the forward flow.

Fig. 16 illustrates the reverse flow stream pattern inside the Tesla valve for different Hartmann numbers. It can be observed that the flow becomes more complex with increasing magnetic flux intensity, particularly in the bifurcation zone. As the Hartmann number increases, a noticeable acceleration of the fluid is recorded, especially downstream of the bifurcation region. Before this bifurcation, the streamlines were nearly parallel; applying a magnetic field caused these lines to distort significantly, leading to strong vortical structures in that area. Furthermore, the presence of a magnetic field also promotes a flow stagnation in the curved section of the channel, indicating a strong influence of magnetic field intensity on the reverse flow dynamics.

Fig. 17 presents the streamline, dimensionless velocity, and dimensionless temperature fields in the horizontal plane (1) (see Fig. 8. **(a)**) for various Hartmann numbers. This figure confirms the previous observations related to the three-dimensional flow structure. Indeed, the Hartmann number significantly reduces flow dimensionless velocity in the curved section of the channel by inducing strong vortex formations. In the case of Ha = 100, two vortices have been developed at the level of the inlet and the outlet of the curved channel part, forming hydrodynamic barriers that stop the fluid flow in this part. The Tesla valve, thus, loses its diode behavior in this situation, as the curved region becomes almost stagnant. Consequently, the Tesla valve becomes permeable to reverse flow. It allows the fluid to pass more easily in the reverse direction, especially as the Hartmann number increases and the dimensionless velocity is in this reverse path.

Regarding the thermal behavior in the reverse flow configuration, a phenomenon similar to that of the forward flow case has been observed, with hot fluid accumulating in the curved channel.

We analyzed several cross-sectional planes better to understand the thermal and hydrodynamic structures inside the channel. Beginning with the plane (2) passing through the curved channel (see Fig. 8. **(b)**) illustrated in Fig. 18, no Dean vortices have been observed, indicating a significant reduction in flow intensity within this region in this case of flow, especially as the Hartmann number increases. Moving to the cross-section of the plane (3) (see Fig. 8. **(c)**) presented in Fig. 19, the introduction of the magnetic field promotes the formation of a co-rotating vortex, although accompanied by a drop in local flow dimensionless velocity. At this location, the thermal evolution is characterized by an expansion of the thermal boundary layer in the direction of the Lorentz force.

Fig. 20 shows the dimensionless pressure distribution along the two straight channels of the Tesla valve for various Hartmann numbers in

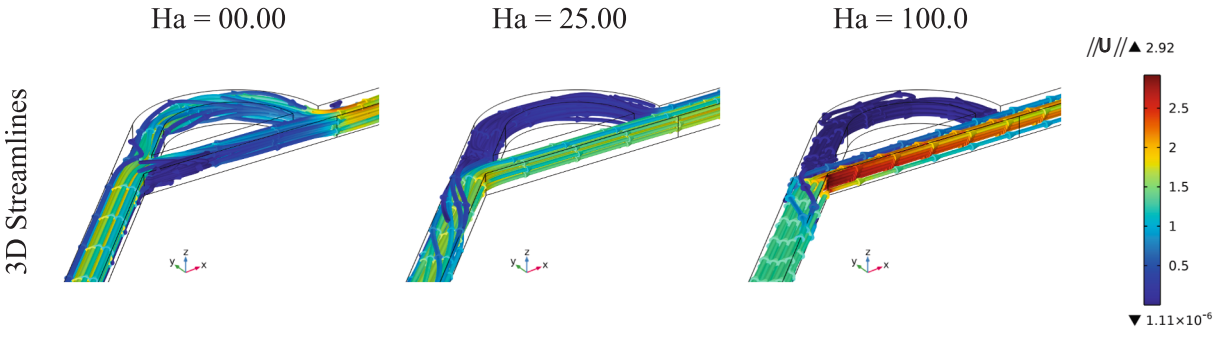

Fig. 16. Flow streamlines colored with the dimensionless velocity magnitude in the case of reverse flow for different Hartmann numbers at Re = 500, Ri = 0, and φ = 0.04.

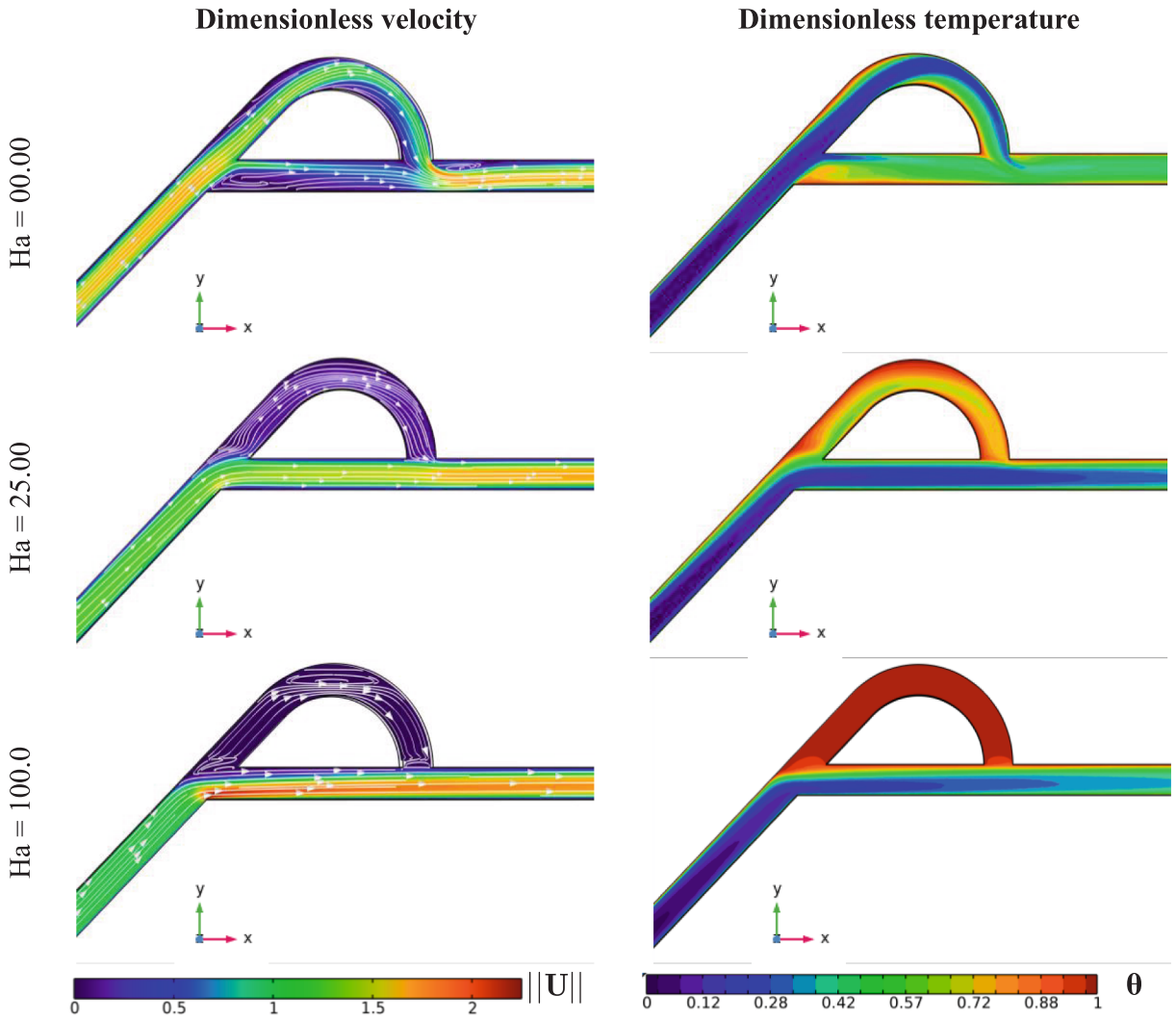

Fig. 17. Dimensionless velocity and temperature distribution in the measurement plane 1 in the case of reverse flow for different Hartmann numbers at Re = 500, Ri = 0, and φ = 0.04.

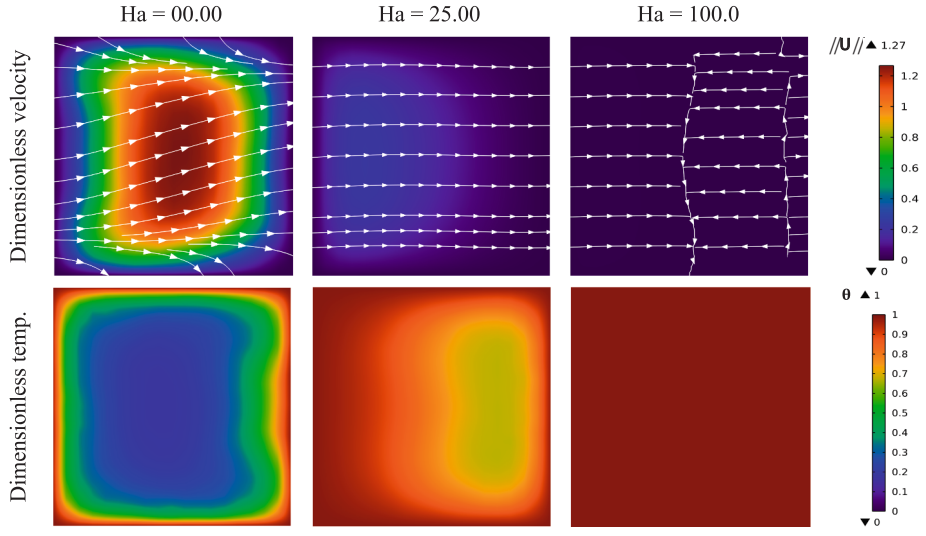

Fig. 18. Dimensionless velocity and temperature distribution in the measurement plane 2 in the case of reverse flow for different Hartmann numbers at Re = 500, Ri = 0, and φ = 0.04.

reverse flow. It is observed that increasing the Hartmann number leads to a rise in static dimensionless pressure along the first straight channel

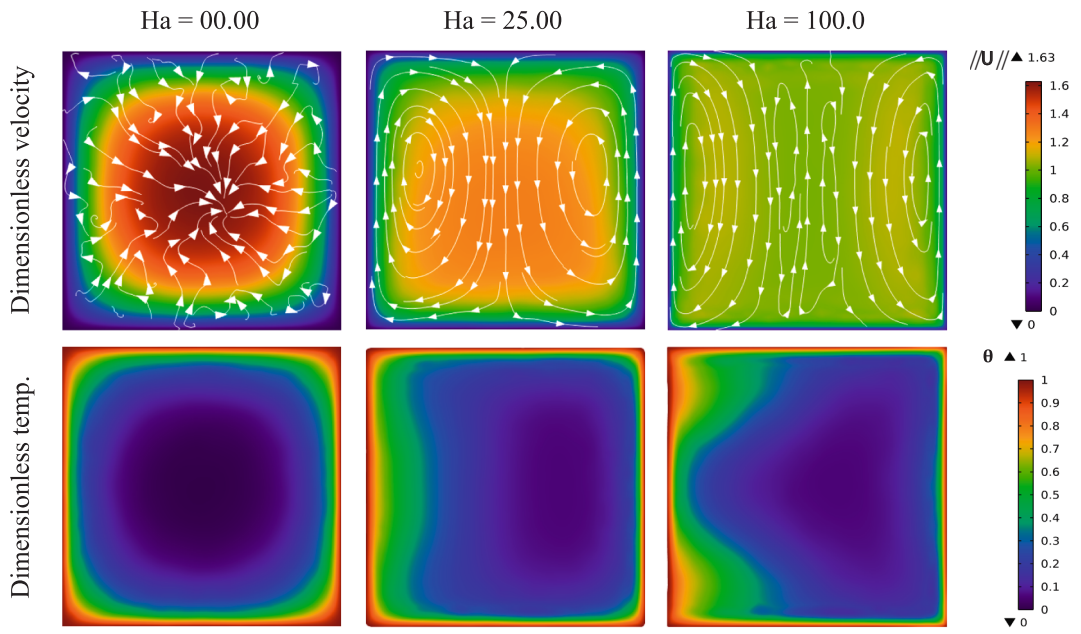

Fig. 19. Dimensionless velocity and temperature distribution in the measurement plane 3 in the case of reverse flow for different Hartmann numbers at Re = 500, Ri = 0, and φ = 0.04.

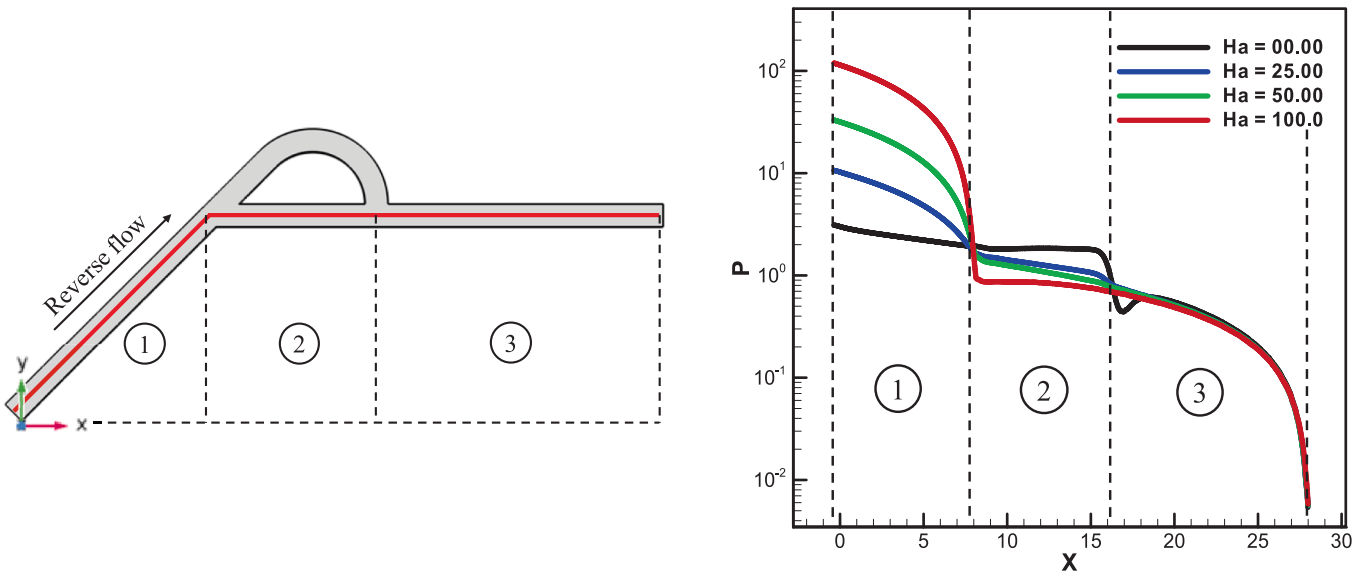

Fig. 20. Dimensionless pressure distribution along the measurement line in the case of reverse flow for different Hartmann numbers at Re = 500, Ri = 0, and φ = 0.04.

(zone 1) with about 150 % in the case of Ha = 25 (at the inlet). However, in the curved section, particularly in the second straight channel (zone 2), the dimensionless pressure is locally reduced with higher Hartmann numbers. Beyond this zone (along the zone 3), the influence of the magnetic field weakens, and the flow re-stabilizes, resulting in nearly identical dimensionless pressure profiles for all Hartmann numbers. This indicates that the magnetic field's effect is localized. Once the fluid exits the magnetically influenced region, pressure recovery occurs due to the absence of further electromagnetic resistance, as already shown in Fig. 10.

Based on this hydrodynamic and pressure analyses, it has been observed that the presence of a magnetic field with such an orientation can significantly disrupt the standard operation of the Tesla valve. Indeed, under magnetic influence, the reverse-flow blocking has been weakened compared to the no-field condition. However, in magnetically actuated environments, the reliability of the Tesla valve is commonly assessed through the diodicity parameter, which quantifies the deviation of the reverse-flow behavior relative to the forward-flow reference.

5.4. *Pressure drops and diodicity*

The pressure drop reflects the inlet pressure (maximal), since a dimensionless relative pressure of zero has been imposed at the outlet as a boundary condition.

Fig. 21 shows the evolution of the dimensionless pressure drop across the Tesla valve as a function of the Hartmann number for both forward and reverse flow configurations. It is observed that, regardless of the Hartmann number, the most important dimensionless pressure drops have been observed in the case of the reverse flow. In addition, the difference between the dimensionless pressure drops in the two cases

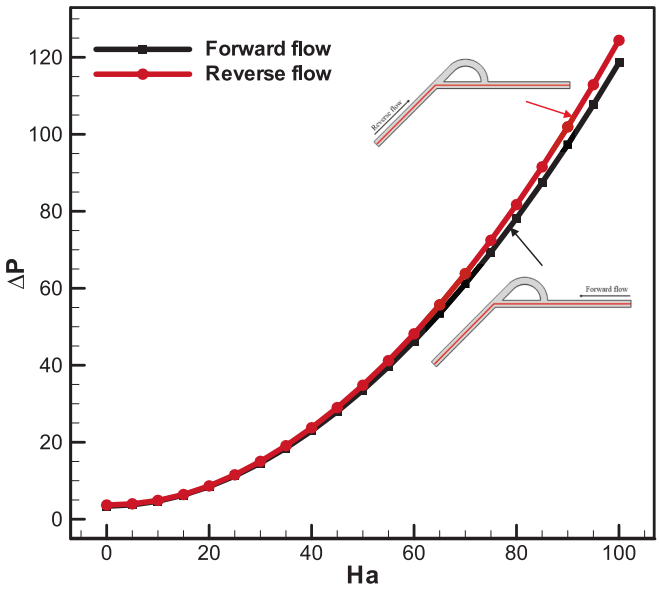

Fig. 21. Dimensionless pressure drops as a function of Hartmann number in the case of forward and reverse flow for different Hartmann numbers at Re = 500, Ri = 0, and φ = 0.04.

(forward and reverse flows) becomes more pronounced as the Hartmann number increases. As expected from magnetohydrodynamic principles, increasing the Hartmann number leads to a significant rise in the dimensionless pressure drop due to the intensified Lorentz force, which acts in the present flow as a promoting force, hence the nanofluid flow rate.

The diodicity is a key parameter for the Tesla valve as it effectively reflects its reliability by quantifying the flow response in both directions according to the same flow and operating conditions.

Fig. 22 illustrates the evolution of the diodicity as a function of Hartmann numbers. It is observed that upon the initial application of a magnetic field (even at low magnetic flux densities), the diodicity tends to decrease abruptly within the range of Hartmann numbers from Ha = 0 to approximately Ha ≈ 17. Beyond this point, the diodicity gradually increases in a logarithmic manner, reaching higher values up to a

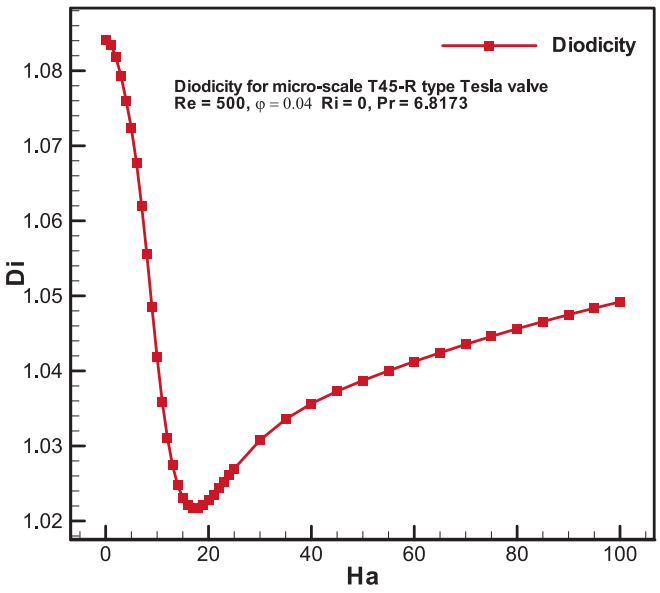

Fig. 22. Diodicity as a function of Hartmann number at Re = 500, Ri = 0, and φ = 0.04.

Hartmann number of Ha = 100. Nevertheless, this increase does not reach the diodicity level observed without a magnetic field (Ha = 0). Indeed, in the interval between Ha = 0 and 17, the dimensionless pressure drops at a rising rate as a function of the Hartmann number in the case of forward flow ($\Delta(\Delta P_f)/\Delta Ha$) is more critical than that of the reverse flow ($\Delta(\Delta P_r)/\Delta Ha$). In other words, the pressure drops in response to the magnetic field for forward flow to rise faster than reverse flow. The faster increase of forward flow dimensionless pressure drops compared to the reverse flow at low Hartmann numbers (Ha < 17) arises from the direct action of the Lorentz force on the forward flow, efficiently reducing viscous losses. Beyond the Hartmann number of Ha ≈ 17, the diodicity increases due to the faster rise of the reverse flow dimensionless pressure drops responding to the magnetic field, making the effect of the magnetic field similar to that of inertial forces (fluid momentum) [37].

In the present study, we have employed a specific type of iron oxide, known as magnetite (Fe_3O_4), suspended in water to highlight its hydrodynamic and thermal impact within the Tesla valve. However, it is essential to understand the effect of nanoparticle concentration on the Tesla valve's overall performance. Therefore, it has been deemed necessary to analyze the pressure drop for both forward and reverse flows and diodicity, as a function of four different concentrations: 0 (pure water), 0.04, 0.08, and 0.1, under various Hartmann numbers.

Due to the dimensionless approach adopted in the present study, where pressure has been normalized through the division by the nanoparticle density (**Eq.** (14)), the previously presented dimensionless pressure drop does not effectively reflect the influence of the nanoparticles. To accurately highlight the effect of nanoparticles concentration on the pressure drops, it is essential to apply a correction factor. Specifically, the dimensionless pressure drops ΔP must be multiplied by a corrective coefficient equal to the ratio of the nanofluid density to that of the base fluid (ρ_{nf}/ρ_f) [67].

Fig. 23 shows the variation of the modified dimensionless pressure drop as a function of Hartmann number for different volume fractions of magnetite nanoparticles, considering both forward and reverse flows. It is observed that, regardless of the flow direction, increasing the nanoparticle volume fraction increases the modified dimensionless pressure drop. The highest values are consistently recorded for reverse flow. This behavior is attributed to the nanofluid's enhanced effective viscosity and density due to the presence of magnetite nanoparticles. As the concentration increases, the flow resistance rises, resulting in a greater modified dimensionless pressure drop.

Fig. 24 illustrates the variation of diodicity as a function of the Hartmann number for different volume fractions of magnetite nanoparticles. While the general shape of the curves remains nearly identical regardless of the nanoparticle concentration, a closer examination reveals some subtle differences. For lower Hartmann numbers (Ha < 20), increasing the nanoparticle volume fraction leads to a slight enhancement in diodicity. This is due to the increase in effective viscosity and magnetization of the fluid, which enhances the flow rectification mechanism in the Tesla valve. However, for higher Hartmann numbers, the influence of nanoparticle concentration becomes less significant. This is likely because the magnetic field dominates the flow behavior, and the additional magnetic response becomes saturated due to concentration. On the other hand, all diodicity curves tend to intersect in a narrow range of Hartmann numbers between 21 and 23. This crossing suggests a transitional regime where the combined effects of magnetic field strength and nanoparticle loading reach a balance point beyond which further increases in concentration slightly hinder the rectification efficiency.

5.5. *Heat transfer rate*

The heat transfer efficiency is generally evaluated through the convective heat transfer rate, which is commonly characterized by the dimensionless Nusselt number. Fig. 25 shows the average Nusselt

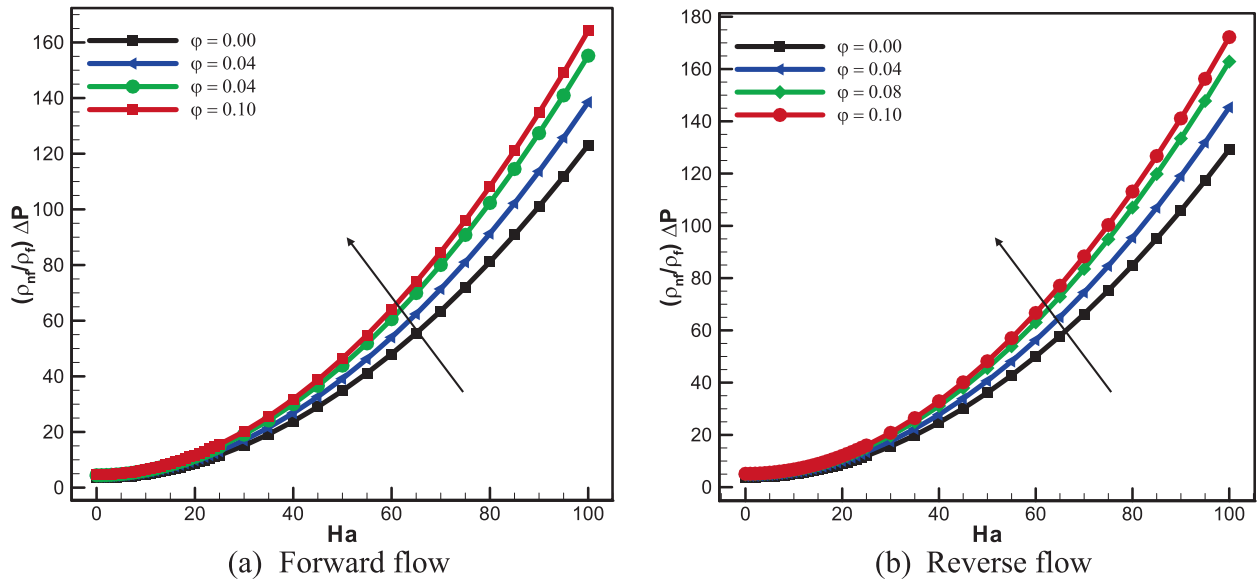

Fig. 23. Modified dimensionless pressure drops as a function of Hartmann number for different nanoparticle volume fractions in forward and reverse flow at Re = 500, Ri = 0.

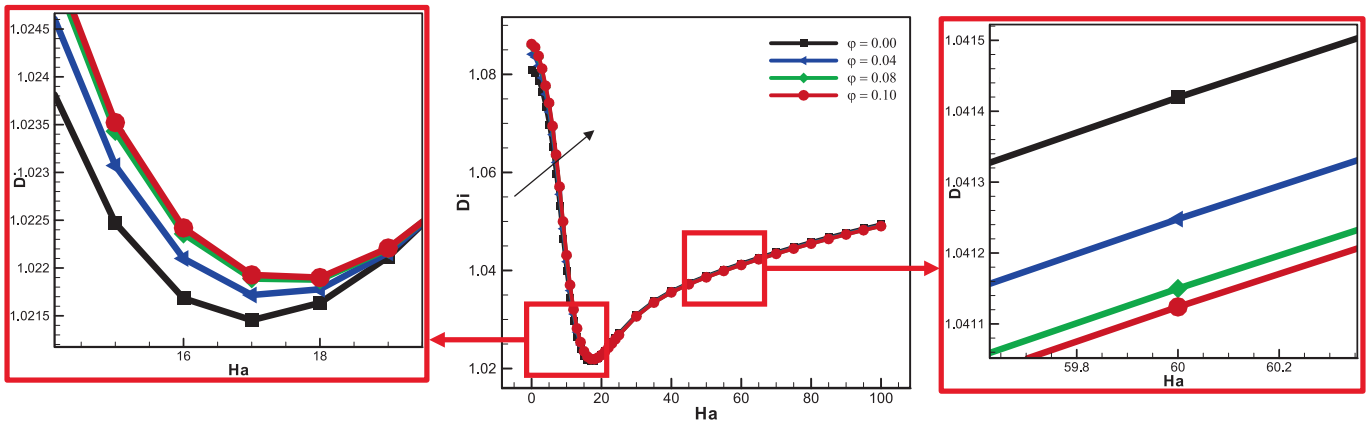

Fig. 24. Diodicity is a function of the Hartmann number for different nanoparticle volume fractions at Re = 500, Ri = 0.

number along the lateral wall of the Tesla valve as a function of the Hartmann number for different nanoparticle volume fractions, considering both forward and reverse flow directions. In general, the Nusselt number exceeds the value of 1 for all cases, confirming that convective heat transfer dominates over pure conduction. Without a magnetic field (Ha = 0), the reverse flow configuration exhibits a higher Nusselt number than the forward flow.

For the forward flow, increasing both the Hartmann number and nanoparticle concentration results in a significant enhancement of heat transfer, as reflected by the increasing Nusselt number. This behavior is particularly pronounced for Ha < 25–30, where the Lorentz force enhances flow alignment and promotes boundary layer thinning, thus improving convective heat exchange. At higher Hartmann numbers (Ha > 30), the Nusselt number increase rate becomes more moderate. Conversely, in the reverse flow case, introducing a magnetic field initially causes a rapid and substantial drop in the average Nusselt number for all volume fractions. Indeed, as Ha increases toward Ha ≈ 20, this magnetic field leads to more laminar and less effective heat transfer. However, beyond Ha ≈ 20, the Nusselt number begins to rise again. This increase is due to the dominance of magnetoconvection. At sufficiently high magnetic field strengths, the flow is restructured to align thermal gradients with more efficient heat transport paths, and the added thermal conductivity from nanoparticles starts to play a more significant role again. This dual behavior underscores the complex interplay between magnetic damping, flow topology, and nanoparticle-enhanced thermal conduction, which varies notably between forward and reverse flow regimes.

6. Conclusion

In this work, a numerical investigation of ferromagnetic nanofluid Fe_3O_4-water flow and heat transfer within a Tesla microvalve subjected to various intensities of an external uniform magnetic field has been conducted. The study aimed to understand the complex interplay between hydrodynamic behavior, thermal performance, and the magnetohydrodynamic effects induced by applying a uniform horizontal magnetic field. Particular attention has been given to both forward and reverse flow configurations to assess the directional selectivity (diodicity) and thermal control capabilities of the Tesla valve when operating with magnetically responsive nanofluids. Based on the detailed simulations and analysis, the following key conclusions have been drawn:

- The presence of a magnetic field strongly influences the internal flow topology, especially in the curved section of the Tesla valve. The

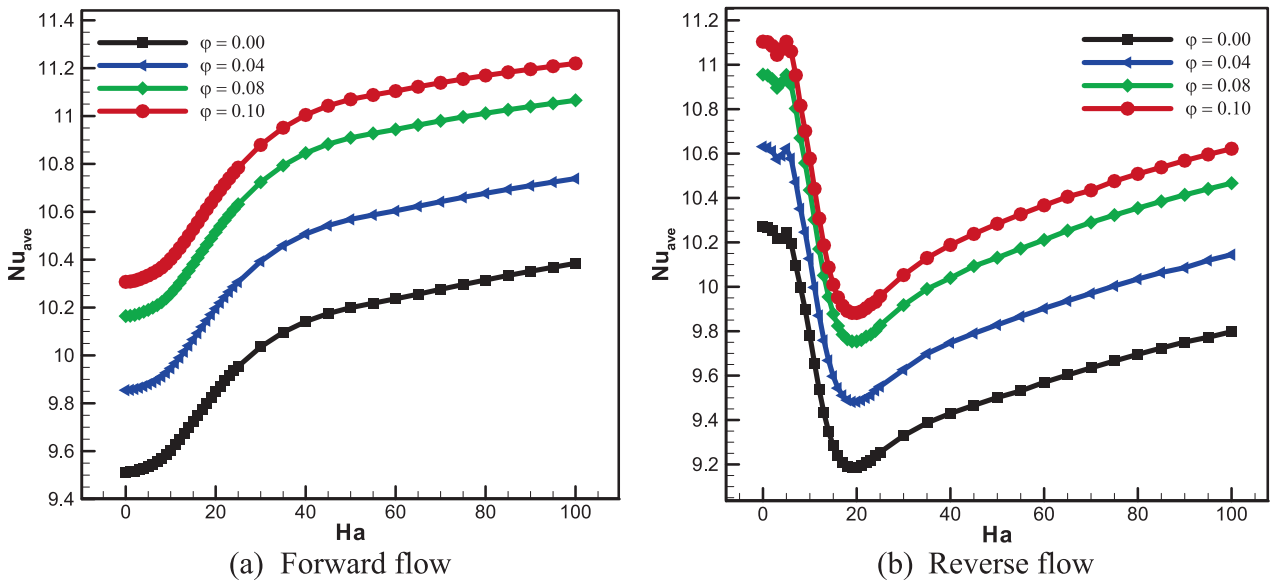

Fig. 25. Average Nusselt number as a function of Hartmann number for different nanoparticles volume fractions in the case of forward and reverse flow at Re = 500, Ri = 0.

Lorentz force disrupts or stabilizes vortices depending on the flow direction and magnetic intensity, leading to three-dimensional, magnetically controlled vortex formations.

- The magnetic field significantly affects both flow directions, inducing a pressure difference that increases by nearly 150 % for moderate magnetic flux densities (Ha ≈ 25) compared to the non-magnetic case
- In the forward direction, the magnetic field applied along the x-axis promotes organized streamlines and suppresses undesired recirculation and fluid stagnation in the curved part of the channel. This enhances the Tesla valve's functionality by stimulating a strong forward flow and improving heat transfer efficiency by thinning the thermal boundary layers.
- In the reverse flow direction, the x-direction magnetic field induces significant flow stagnation and vortex formation within the curved part of the channel. At high Hartmann numbers, these regions become completely blocked. However, when the magnetic field is applied in such a direction, it facilitates and promotes the reverse flow, reducing the Tesla valve's efficiency.
- The Tesla valve diodicity exhibits a nonlinear evolution with the Hartmann number. Initially decreasing due to disproportionate magnetic braking of forward flow, it then increases steadily beyond Ha ≈ 17, confirming the valve's ability to favor forward over reverse flow in high magnetic regimes. However, the absence of a magnetic field represents the optimal operating condition, as even increasing the magnetic flux density does not achieve diodicity values as high as those obtained without any magnetic field.
- Increasing the volume fraction of magnetite nanoparticles leads to a greater pressure drop due to enhanced viscosity and density, but also improves diodicity at low Hartmann numbers (Ha < 20–30) by reinforcing the magnetic responsiveness of the nanofluid.
- The Nusselt number increases significantly with magnetic field intensity and nanoparticle loading in the forward direction, especially for Ha < 30, where the Lorentz force boosts rapidly the convection heat transfer. In reverse flow, despite an initial degradation in heat transfer rate with Ha < 20, magnetoconvection reactivates thermal performance at high Hartmann number.
- The Tesla valve exhibits high tunability through magnetic field intensity and nanoparticle concentration. This enables tailored control over flow directionality and heat transfer efficiency, offering potential for smart flow regulation in microscale systems.
- In general, this study has demonstrated that it is possible to exploit magnetic fields directed in controlled orientations to enhance the effectiveness of Tesla valves by promoting forward flow and suppressing reverse flow. However, it is essential to exercise caution, as magnetic fields may also unintentionally enhance reverse flow, undermining the core function of Tesla valves, namely, the suppression of backward flow. This consideration is especially critical in microscale systems operating in environments susceptible to magnetic field leakage, such as those in microelectronic cooling devices.

7. Limitations and Perspectives

This study provides significant insights into the functional behavior of a T45R Tesla microvalve under a horizontally applied magnetic field aligned with the reverse flow direction and parallel to the curved section of the valve. However, a key limitation lies in restricting this specific magnetic orientation. Moreover, the present formulation assumes a steady-state Newtonian behavior and employs a Fe_3O_4-based ferronanofluid as the working medium, which limits the generality of the findings.

A compelling future direction would be to generalize the magnetic field application by varying its orientation according to the spherical coordinate angles θ and φ, enabling a broader assessment of anisotropic magnetohydrodynamic effects. Additionally, exploring other electrically conductive working fluids such as liquid metals or highly ionized electrolytes could provide deeper insight into the sensitivity of Tesla microvalves to different magneto-fluidic properties. Incorporating buoyancy-driven forces would further transform the problem into a mixed-convection configuration, opening new avenues for understanding complex thermal–magnetic–hydrodynamic interactions in next-generation microvalve systems.

CRediT authorship contribution statement

Abderrahim Mokhefi: Writing – original draft, Visualization, Software, Methodology, Investigation, Conceptualization. **Eugenia Rossi di Schio:** Writing – review & editing, Validation, Supervision, Methodology, Formal analysis, Conceptualization. **Sarra Youcefi:** Writing – original draft, Software, Methodology, Investigation, Conceptualization. **Paolo Valdiserri:** Writing – review & editing, Validation, Supervision, Methodology, Investigation, Conceptualization.

Declaration of competing interest

The authors declare that they have no known competing financial interests or personal relationships that could have appeared to influence the work reported in this paper.

References

[1] Bardell RL. The diodicity mechanism of Tesla-type no-moving-parts valves. Diss: University of Washington; 2000.
[2] Shellock FG. Prosthetic heart valves and annuloplasty rings: assessment of magnetic field interactions, heating, and artifacts at 1.5 Tesla. J Cardiovasc Magn Reson 2001;3(4):317–24.
[3] Forster, F.K., Williams, B.E. Parametric design of fixed-geometry microvalves : The tesser valve. *ASME International Mechanical Engineering Congress and Exposition*. Vol. 36576. 2002.
[4] Tesla, N. (1920). *Valvular conduit*. U.S. Patent No. 1,329,559. United States Patent and Trademark Office. https://patents.google.com/patent/US1329559A.
[5] Bardell RL. The diodicity mechanism of tesla-type no-moving-parts valves. Diss: University of Washington; 2000.
[6] Wang Y, Lin Z, Wang B, Liu C, Cai G, Liu H, et al. Two-stage day-ahead and intraday low-carbon dispatch method based on enhancing the peak-load regulation capability of cogeneration units with a novel multi-stage Tesla valve thermal storage device. Energy 2025;316:134467.
[7] Hai T, Rahman MA, Aksoy M, Zhou J, Alenazi MJ, Singh NSS, et al. Investigating the performance of the Tesla valve channel in a photovoltaic thermal system through numerical simulation: Evaluation from the standpoint of thermodynamic laws. Int Commun Heat Mass Transfer 2024;159:108197.
[8] Xiong M, Yang J, Ding X, Li H, Zhang H. Topology optimization design of micromixer based on principle of Tesla valve: an experimental and numerical study. Chemical Engineering and Processing-Process Intensification 2023;193:109560.
[9] Liu Z, Han Q, Han J, Zhang Y, Chen X, Li W. Flow boiling in a relatively large copper heat sink comprised of Tesla microchannels. Int J Heat Mass Transf 2025;236:126366.
[10] Li W, Yang S, Chen Y, Li C, Wang Z. Tesla valves and capillary structures-activated thermal regulator. Nat Commun 2023;14(1):3996.
[11] Gamboa, A. R., & Forster, F. K. (2004, January). Is there a best fixed-geometry valve for micropumps?. In *ASME International Mechanical Engineering Congress and Exposition* (Vol. 47098, pp. 319-324).
[12] Gamboa, A. R., Morris, C. J., & Forster, F. K. (2003, January). Optimization of the fixed-geometry valve for increased micropump performance. In *ASME International Mechanical Engineering Congress and Exposition* (Vol. 37165, pp. 525-534).
[13] Purwidyantri A, Prabowo BA. Tesla valve microfluidics: the rise of forgotten technology. Chemosensors 2023;11(4):256.
[14] Truong TQ, Nguyen NT. Simulation and optimization of tesla valves. Nanotech 2003;1:178–81.
[15] Thompson, S. M., Jamal, T., Paudel, B. J., & Walters, D. K. (2013, November). Transitional and turbulent flow modeling in a tesla valve. In *ASME International Mechanical Engineering Congress and Exposition* (Vol. 56321, p. V07BT08A027). American Society of Mechanical Engineers.
[16] Babaoğlu NU, Parvaz F, Foroozesh J, Hosseini SH, Ahmadi G, Elsayed K. Analysis and optimization of multistage Tesla valves by computational fluid dynamics and a multi-objective genetic algorithm. Chem Eng Technol 2022;45(12):2245–53.
[17] Liu Z, Shao WQ, Sun Y, Sun BH. Scaling law of the one-direction flow characteristics of symmetric Tesla valve. Eng Appl Comput Fluid Mech 2022;16(1):441–52.
[18] Zhang YL, Tong JB, Zhu ZC. Numerical calculation of forward and reverse flow in Tesla valves with different longitudinal width-to-narrow ratios. Sci Rep 2023;13(1):12496.
[19] Zeidan M, Németh M, Abhijith GR, Wéber R, Ostfeld A. Transient flow dynamics in tesla valve configurations: insights from computational fluid dynamics simulations. Water 2024;16(23):3492.
[20] Gan R, Pei Z, Li B. Aerodynamics noise analysis inside multi-stage Tesla valves for superheated steam decompression. Phys Fluids 2025;37(7).
[21] Jang DS, Ham SH, Shin HH, Kim Y. Thermal performance improvement of a radial pulsating heat pipe with diverging channels by adopting Tesla valves at various heat fluxes. Appl Therm Eng 2024;237:121799.
[22] Lu Y, Wang J, Liu F, Liu Y, Wang F, Yang N, et al. Performance optimisation of Tesla valve-type channel for cooling lithium-ion batteries. Appl Therm Eng 2022;212:118583.
[23] Porwal PR, Thompson SM, Walters DK, Jamal T. Heat transfer and fluid flow characteristics in multistaged Tesla valves. Numer Heat Transf A Appl 2018;73(6):347–65.
[24] Huang F, Ren L, Xie S, Leng M, Liao P. Numerical study of flow characteristics and heat transfer mechanism in Tesla valve tube. Results Eng 2024;21:101795.
[25] Cheng P, Jianjun X, Kumar J, Almujibah H, Ali HE, Alkhalifah T, et al. Improving efficiency and optimizing heat transfer in a novel tesla valve through multi-layer perceptron models. Case Stud Therm Eng 2023;49:103391.
[26] Paudel BJ, Jamal T, Thompson SM, Walters DK. Thermal effects on micro-sized tesla valves. InFluids Engineering Division Summer Meeting 2014 Aug 3 (Vol. 46261, p. V002T19A006). American Society of Mechanical Engineers.
[27] Eastman JA, Phillpot SR, Choi SUS, Keblinski P. Thermal transport in nanofluids. Annu Rev Mat Res 2004;34(1):219–46.
[28] Sun W, Liu Y, Xu W, Kan L, Liu H, Zhao L, et al. Study on interaction mechanism between natural convection and forced convection during storage and temperature rise of waxy crude oil tank. Eng Appl Comput Fluid Mech 2025;19(1):2498354.
[29] Kehuan WANG, Xiaofeng LIU, Genchang WANG. Self-scheduled direct thrust control for gas turbine engine based on EME approach with bounded parameter variation. Chin J Aeronaut 2025;103392.
[30] Akhtar Y, Ahmad S, Khalifa HAEW, Hendy AS, Yousif BAA, Idress R. Numerical Investigation of Drug delivery Mechanisms in Pulsatile Flow with Machine Learning Approach. Int J Thermophys 2025;46(3):44.
[31] Ullah S, Saddiq G, Majeed AH, Alotaibi H, Hendy AS, Ali MR. Computational study of conjugate heat transfer and entropy generation of hybrid nano-particles in an enclosure with solid block. Case Stud Therm Eng 2025;67:105822.
[32] Rossi di Schio E, Celli M, Barletta A. Effects of Brownian diffusion and thermophoresis on the laminar forced convection of a nanofluid in a channel. J Heat Transfer 2014;136(2):022401.
[33] Majeed AH, Mahmood R, Liu D, Zhang Y, Zhang JY, Ren HY, et al. Effects of oscillation on convective thermal flow in a vertical enclosure filled by nanofluid particles. Case Stud Therm Eng 2024;61:105133.
[34] Majeed AH, Liu D, Ali AR, Alotaibi H, Yin ZJ, Yi RH. Numerical simulations of energy storage performance in a close configuration: a Galerkin finite element-based computation. Alex Eng J 2024;104:56–65.
[35] Majeed AH, Mahmood R, Liu D. Finite element simulations of double diffusion in a staggered cavity filled with a power-law fluid. Phys Fluids 2024;36(3).
[36] Majeed AH, Mahmood R, Shahzad H, Pasha AA, Islam N, Rahman MM. Numerical simulation of thermal flows and entropy generation of magnetized hybrid nanomaterials filled in a hexagonal cavity. Case Stud Therm Eng 2022;39:102293.
[37] Qian JY, Chen MR, Liu XL, Jin ZJ. A numerical investigation of the flow of nanofluids through a micro Tesla valve. J Zheijang Univ Sci A 2019;20(1):50–60.
[38] Liosis C, Sofiadis G, Karvelas E, Karakasidis T, Sarris I. A Tesla valve as a micromixer for Fe3O4 nanoparticles. Processes 2022;10(8):1648.
[39] Soltani A, Pourfallah M, Sabour SMJS. Thermal enhancement of PEM fuel cell cooling with novel configurations of Tesla valve and hybrid nanofluids: a numerical study. Int J Hydrogen Energy 2024;69:1263–75.
[40] Shahsavar A, Hasani M, Alizadeh AA. Two-phase simulation of hydrothermal performance and entropy generation aspects of a biologically prepared nanofluid-cooled heat sink with helical Tesla valve-based microchannels. Case Stud Therm Eng 2024;58:104429.
[41] Ren F, Li Q, Wang P. Multi-objective optimization of Tesla valve channel battery cold plate with nanofluid by RSM and NSGA-II. J Storage Mater 2025;115:115969.
[42] Hussain S, Ahmed SE. Unsteady MHD forced convection over a backward facing step including a rotating cylinder utilizing Fe3O4-water ferrofluid. J Magn Magn Mater 2019;484:356–66.
[43] Toumi M, Bouzit M, Bouzit F, Mokhefi A. MHD forced convection using ferrofluid over a backward facing step containing a finned cylinder. Acta Mechanica et Automatica 2022;16(1):70–81.
[44] Mokhefi A, Rossi di Schio E. Effect of a magnetic field on the Couette forced convection of a Buongiorno's nanofluid over an embedded cavity. JP Journal of Heat and Mass Transfer 2022;30:89–104.
[45] Amrani K, Rossi Di Schio E, Bouzit M, Mokhefi A, Aris A, Belhout C, et al. Numerical Investigation of the Influence of a magnetic Field on the Laminar Flow of a Yield-stress Nanofluid over a Backward Facing step. Frontiers in Heat and Mass Transfer 2025;23(1):185–206.
[46] Benyamina M, Mokhefi A. Enhancement of thermal and entropy performance of a CPU heatsink using hybrid nanofluid under natural magnetohydrodynamic convection. Journal of the Serbian Society for Computational Mechanics 2024;18(2).
[47] Liu, W., Zhang, X., Cao, Z., Fang, K., & Yang, X. (2024, October). Comparative analysis of performance of different types of Tesla valves. In *Journal of Physics: Conference Series* (Vol. 2854, No. 1, p. 012103). IOP Publishing.
[48] Ahmad S, Liu D, Majeed AH. MHD double diffusive flow analysis in a permeable cavity: an endothermic versus exothermic based study. Int Commun Heat Mass Transfer 2025;162:108604.
[49] Karimipour A, Taghipour A, Malvandi A. Developing the laminar MHD forced convection flow of water/FMWNT carbon nanotubes in a microchannel imposed the uniform heat flux. J Magn Magn Mater 2016;419:420–8.
[50] Bahmani M, Babagoli M, Jalili P, Jalili B, Ganji DD. The numerical study on the MHD natural convection trend of square/circle corrugated porous media. Journal of Engineering Research 2024.
[51] He D, Xu H, Wang Y, Wang M, Duan Z, Yang N, et al. Research on vertical vibration characteristics of rolling mill based on magnetorheological fluid damper absorber. Mech Syst Sig Process 2025;224:112203.
[52] Delannoy Y, Montero I, Zapata A, Machicoane N. Seawater magnetohydrodynamic pumps and thrusters: experiment, model and upscaling. Magnetohydrodynamics C/c of Magnitnaia Gidrodinamika 2025;61:55–66.
[53] Daus JJ. *Magnetohydrodynamic Induction Pump Jet Propuslor for Undersea Vehicles*. Massachusetts Institute of Technology); 2024. Doctoral dissertation.
[54] Rajesh V, Öztop HF. Conjugate MHD natural convection in a chamber filled by ternary hybrid nanofluid with entropy generation. Numer Heat Transf A Appl 2025;86(19):6671–92.
[55] Lihonou TF, Diakite M, Laouer A, Segning H, Mathos KP, Camara N. Analysis of Heat and Mass transfer in MHD Forced Convection with Chemical Parameter Effects on a Horizontal Porous Plate. Braz J Phys 2025;55(6):275.
[56] Adogbeji VO, Atofarati EO, Sharifpur M, Meyer JP. Magnetohydrodynamics of nanofluid internal forced convection: a review and outlook for practical applications. Results Phys 2025;68:108082.

[57] Raza Q, Ali B, Ghazwani HA, Younis J. ANN-based modeling of porous MHD mixed convection in tri-hybrid nanofluids with thermal radiation. J Radiat Res Appl Sci 2025;18(3):101852.
[58] Abdelli N, Sahi A, Benaouicha M, Guillou S, Öztop HF, Adnani M, et al. Numerical study of MHD thermo-convective flows in a square cavity with a deformable wall: effects of heating plate inclination. J Therm Anal Calorim 2025;150(16):12369–89.
[59] Mokhefi A, Youcefi S, Valdiserri P, di Schio ER. Magnetic field influence on the stabilization of an elastic fin under natural convection in a square cavity with nanofluids. Therm Sci Eng Prog 2025;104258.
[60] Iqbal K, Rossi di Schio E, Anwar MA, Razzaq M, Shahzad H, Valdiserri P, et al. A Fluid–Structure Interaction Analysis to Investigate the Influence of magnetic Fields on Plaque Growth in Stenotic Bifurcated arteries. Dynamics 2024;4(3):572–91.
[61] Haghparast M, Alizadeh Pahlavani MR. Experimental and numerical analysis of 3D end effects in Naval Magnetohydrodynamic propulsion motors. Journal of Marine Engineering & Technology 2024;23(5):373–81.
[62] Ganji DD, Mahboobtosi M, Chari FN. Investigation of time-dependent magnetohydrodynamic flow and heat transfer of compressed penta-hybrid nanofluids: Biomedical applications. J Radiat Res Appl Sci 2025;18(4):101915.
[63] Derbal, D., Bouzit, M., Mokhefi, A., & Bouzit, F. (2024, February). Numerical Investigation of the Magnetohydrodynamic Mixed Convection inside an Extended Curved Duct in the Presence of a Nanofluid of Different Metallic Oxides Nanoparticles. In *Defect and Diffusion Forum* (Vol. 430, pp. 107-132). Trans Tech Publications Ltd.
[64] Derbal D, Bouzit M, Mokhefi A, Bouzit F. Numerical analysis of a nanofluid behavior in an expanded curved duct using the two-phase Buongiorno model. J Therm Anal Calorim 2023;148(20):11131–54.
[65] Barletta A, Rossi di Schio E, Celli M. Convection and instability phenomena in nano-fluid-saturated porous media. Heat Transfer Enhancement with Nanofluids, CRC Press, Boca Raton, FL 2015;341:364.
[66] Rossi di Schio E, Impiombato AN, Mokhefi A, Biserni C. Theoretical and Numerical Study on Buongiorno's Model with a Couette Flow of a Nanofluid in a Channel with an embedded Cavity. Appl Sci 2022;12(15):7751.
[67] Mokhefi A, Bouanini M, Elmir M. Numerical simulation of Laminar Flow and Heat transfer of a Non-Newtonian Nanofluid in an Agitated Tank. International Journal of Heat & Technology 2021;39(1).